universe

MDPI

Review

Extracting Phase Structure and Stability of the Magnetic Dual Chiral Density Wave from a Ginzburg–Landau Expansion

William Gyory [1,2]

[1] Department of Physics and Astronomy, Iowa State University, Ames, IA 50011, USA; wgyory@asu.edu
[2] College of Integrative Sciences and Arts, Arizona State University, Phoenix, AZ 85212, USA

Abstract

We review some recent findings on thermal properties of the magnetic dual chiral density wave (MDCDW) condensate in the Nambu–Jona-Lasinio (NJL) model of dense quark matter, as well as a convenient method for investigating this phase with a high-order Ginzburg–Landau (GL) expansion. We show how a recently discovered formula for the GL coefficients can be used to compute key physical properties of the condensate, such as its ground state order parameters and critical temperature in the mean-field approximation and its stability against thermal phonon fluctuations. We find that magnetic fields of order 10^{18} G significantly increase the condensate magnitude and critical temperature, eventually making the condensate favored up to temperatures a few times 10 MeV over the entire range of densities in the model. At much smaller fields, the condensate is still preferred and thermally stable over a range of densities relevant to cold neutron stars. We emphasize how the topological features of MDCDW are encoded in certain terms of the GL expansion, which can be used to show that the preceding effects have a topological origin. Finally, we present a new result on the convergence properties of the GL expansion, proving that it converges when $|m| + |b| < \sqrt{\mu^2 + (\pi T)^2}$, where m and b are order parameters proportional to the condensate magnitude and spatial modulation, respectively. This condition holds over a large region of parameter space, including the region of interest for neutron star applications.

Keywords: dynamical symmetry-breaking models; nuclear astrophysics; nuclear matter in neutron stars; QCD phenomenology; chiral symmetry; spontaneous symmetry breaking

1. Introduction

Quantum chromodynamics (QCD) accounts for 99% of the visible matter in the universe, but its phase diagram in the region of low temperatures and intermediate densities remains poorly understood. The energy scale in this region is too low to apply perturbative methods, while the sign problem obstructs lattice methods. Improving our knowledge of nuclear matter under these conditions is crucial, however, due in part to its relevance to neutron stars (NSs). NSs provide a natural laboratory for probing cold, dense QCD, and they also host extremely strong magnetic fields. The strongest observed surface fields on magnetars reach the order of 10^{15} G, and field strengths at the core remain unknown; upper estimates typically appear on the order of 10^{17}–10^{18} G for neutron matter [1] and 10^{20} G for quark matter [2]. Thus, we have ample motivation to investigate cold, dense QCD in a magnetic field using the best tools available, which usually take the form of approximate models and effective theories. The Nambu–Jona-Lasinio (NJL) model [3,4], for example, gives a low-energy effective description of quark matter with four-point quark interactions,

Check for updates

Academic Editors: Nicolas Chamel and Jorge Segovia

Received: 1 April 2026
Revised: 6 July 2026
Accepted: 7 July 2026
Published: 11 July 2026

Copyright: © 2026 by the author. Licensee MDPI, Basel, Switzerland. This article is an open access article distributed under the terms and conditions of the Creative Commons Attribution (CC BY) license.

and it is commonly used to gain insight into the behavior of symmetry breaking in QCD. The main focus of the current review involves symmetry breaking in the NJL model, which we discuss in more detail in Section 2.1.

Many theoretical studies into the cold and dense region of the phase diagram have found spatially inhomogeneous phases (IPs) to be preferred over homogeneous ones [5]. IPs are ubiquitous in condensed matter physics, with examples including charge and spin density waves [6], mass and spin imbalanced cold atom Fermi gases [7], and crystalline superconducting phases, such as the Fulde–Ferrell–Larkin–Ovchinnikov (FFLO) phase [8,9]. IPs were proposed in the context of nuclear matter as early as 1960 by Overhauser [10], and they have since appeared in the large N_c limit of QCD [11], the sigma model [12], the NJL model [13–15], color superconducting phases [16,17], and quarkyonic matter [18]. Physically, one can understand the tendency toward such phases as the result of a large chemical potential μ giving rise to a Fermi sea. Particle–antiparticle pairs become disfavored due to the energy cost associated with lifting quarks or nucleons to the Fermi surface, but particle–hole pairs with nonvanishing momentum can form at the surface for little energy cost. The net momentum of these particle–hole pairs manifests as spatial inhomogeneity. We offer a few more remarks on this picture in terms of pairing mechanisms in Section 4.1.

As indicated above, several lines of research suggest that IPs are plausible candidates for cold and moderately dense nuclear matter. In fact, so many such phases have been proposed that it is a daunting task to determine which one is energetically favored. In the NJL model in $1+1$ dimensions, the problem turns out to be more tractable: In Ref. [19], Başar et al. were able to solve the gap equation exactly, finding that the most general solution is characterized by a complex order parameter whose phase and amplitude vary according to nontrivial expressions involving Jacobi elliptic functions. This solution has two special limiting cases: the dual chiral density wave (DCDW), which has constant amplitude and a simple spatial modulation, and the real kink crystal (RKC), which has constant phase and whose amplitude varies according to elliptic functions. Of this family of solutions, it was shown that DCDW is favored in the $(1+1)$-dimensional NJL model.

In $3+1$ dimensions, the problem is more difficult. The exact solution to the gap equation in this case is unknown, hence many candidate phases have been proposed and studied. Here, there is also the possibility of multi-modulated phases, which have spatial dependence in several directions. The analogous version of the RKC—often called the solitonic chiral condensate in this setting—has been found to be favored over many other condensates in $3+1$ dimensions without a magnetic field. For example, in Ref. [14], Nickel found this phase to be favored over DCDW when considering single modulations. In Ref. [20], Abuki et al. compared several different condensates and modulation dimensions and also found the single-modulated solitonic condensate to be preferred. Ref. [21] reached a similar conclusion by comparing this solution to condensates with various forms of two-dimensional modulations.

The preference for the solitonic chiral condensate phase in $(3+1)$-dimensional NJL may change when magnetic fields and thermal fluctuations are taken into account. In a strong magnetic field, particles in the lowest Landau level (LLL) have restricted transverse momenta, and hence their dynamics become effectively $1+1$-dimensional. This raises the possibility that magnetic fields will make DCDW become favored, as this phase is known to be the ground state in $1+1$ dimensions. As for thermal fluctuations, it is important to note that almost all of the studies mentioned above are based on the mean-field theory of each condensate. Thermal fluctuations that occur beyond mean-field theory may have drastic consequences for single-modulated condensates, however, due to the Landau–Peierls (LP) instability [22–25]. This phenomenon, in which thermal fluctuations wash out the long-range correlations and effectively erase the condensate at any finite temperature, typically

plagues single-modulated phases in $3+1$ dimensions. However, as first noted in Ref. [26] and as will be discussed later in this article, the LP instability can be avoided in the presence of a magnetic field.

In this paper, we review some recent results on the DCDW condensate in the NJL model in $(3+1)$ dimensions in the presence of a magnetic field—known as the magnetic DCDW (MDCDW) condensate—and we also present a new result on the convergence of its Ginzburg–Landau (GL) expansion. A key feature of this condensate, which distinguishes it from many other IPs in $3+1$ dimensions, is an asymmetry in the spectrum of the lowest Landau level modes. This spectral asymmetry is related via the Atiyah–Patodi–Singer index theorem to a chiral anomaly term in the effective action and is thus topological in origin [27,28]. As a result, MDCDW exhibits several topological effects, such as anomalous charge and transport properties. The spectral asymmetry also generates new terms in the GL expansion that are odd in the spatial modulation, and these terms enhance the condensate's magnitude and critical temperature. Strikingly, these topological terms in the GL expansion also stabilize the condensate against thermal fluctuations, allowing it to avoid the LP instability.

In this review, we focus on how the GL expansion can be used as a systematic tool for the investigation of MDCDW. We highlight in particular the role of the topological terms in the expansion, indicating how one can extract their physical consequences both in mean-field theory and beyond. Finally, we prove a new result on the region of parameter space in which the expansion converges. The paper is organized as follows: In Section 2, we review the background theory of the MDCDW phase and present the formulas for its free energy. In Section 3, we introduce the GL expansion and discuss the coefficient formulas that enable fast calculation of the condensate's phase structure and stability. In Section 4, we give results on the ground-state order parameters and critical temperature in the mean-field approximation. In Section 5, we examine the effect of thermal phonon fluctuations beyond mean-field theory, reviewing the LP instability and showing how MDCDW avoids it. We then present a quantitative version of this result, namely, the threshold temperature at which these fluctuations begin to erase the long-range order of the condensate. In Section 6, we prove that the GL expansion converges when $|m|+|b|<\sqrt{\mu^2+(\pi T)^2}$, where m and b are order parameters proportional to the condensate magnitude and spatial modulation, respectively. This condition is satisfied by the ground state in most of the region of interest, even in some places where the condensate magnitude or spatial modulation parameter are large. We give closing remarks and discuss possible directions for future work in Section 7.

2. Theory of MDCDW

2.1. The NJL Model

We work in a two-flavor NJL model,

$$\mathcal{L}=\bar{\psi}(i\gamma^\mu D_\mu+\gamma^0\mu)\psi+G[(\bar{\psi}\psi)^2+(\bar{\psi}i\tau\gamma_5\psi)^2], \tag{1}$$

where $\psi^T=(u,d)$, $D_\mu=\partial_\mu+iQA_\mu$, $Q=\mathrm{diag}(e_u,e_d)=\mathrm{diag}(\frac{2}{3}e,-\frac{1}{3}e)$, G is the four-fermion coupling constant, and $\tau=(\tau^1,\tau^2,\tau^3)$ are the Pauli matrices acting in isospin space. We assume a fixed background electromagnetic potential $A^\mu=(0,0,Bx,0)$, which corresponds to a constant and uniform magnetic field $\mathbf{B}$ in the z-direction.

Before proceeding to the condensate, we shall provide a brief background on the NJL model. NJL can be considered a low-energy approximation to QCD that integrates out gluon degrees of freedom, replacing tree-level gluon exchange diagrams with four-point quark vertices (historically, however, NJL predates QCD). NJL also replicates the symmetries of QCD, and hence it is useful for studying symmetry breaking. In particular, QCD and NJL exhibit approximate global chiral symmetry, i.e., symmetry under the transformations

$SU(N_f)_L \times SU(N_f)_R$, or equivalently under $SU(N_f)_V : \psi \mapsto e^{i\theta_a^V \tau_a}\psi$ and $SU(N_f)_A : \psi \mapsto e^{i\theta_a^A \gamma_5 \tau_a}\psi$. Chiral symmetry (and its breaking) plays a central role in QCD phenomenology: In vacuum, it is spontaneously broken by the formation of a chiral condensate $\langle\bar{\psi}\psi\rangle = \Delta$, in which left-handed quarks pair with right-handed anti-quarks and vice versa. This symmetry breaking has major consequences: The theory has a nontrivial vacuum state, quarks acquire dynamical mass, and pions arise as Goldstone modes. It should be noted that chiral symmetry is only approximate due to the nonvanishing quark current masses. However, the up and down quark masses are small relative to the condensate magnitude, so their effects may be treated as corrections to the chiral limit, in which quark masses vanish and chiral symmetry is exact. Many NJL model analyses of dense quark matter, including the present one, work in the chiral limit.

Because NJL replicates symmetries that are crucial to the phenomenology of QCD, it is typically thought to offer insight into the behavior of genuine QCD at low energies, at least in terms of its phase transitions and symmetry restoration on a schematic level [29]. However, it is also worth noting the limitations of the model. Because it lacks gluons, NJL also lacks confinement, a core feature of QCD in the hadronic phase. The four-fermion interactions also render the theory non-renormalizable, so it must be regulated with an ultraviolet (UV) cutoff. Many regularization schemes are common in the literature [30], and some predictions have been shown to be sensitive to the regularization scheme adopted [31]. We discuss regularization in more detail the next subsection.

In light of these shortcomings, NJL can be viewed as a low-energy effective theory of quarks that should not be trusted above a certain energy scale. It has therefore been used extensively in studies of cold and dense quark matter at moderate densities, where confinement and gluon degrees of freedom should be negligible.

2.2. The MDCDW Condensate

The MDCDW condensate is defined by the ansatz

$$-2G\Big(\langle\bar{\psi}\psi\rangle + i\langle\bar{\psi}i\gamma^5\tau_3\psi\rangle\Big) = me^{i2bz} = M(z), \tag{2}$$

where we have introduced order parameters m and b, which are proportional to the condensate magnitude and spatial modulation in the z-direction, respectively. Physically, m is the effective mass of the fermion quasiparticles in the condensate background, and b is the momentum of a particle in a quark–hole pair. The magnetic field explicitly breaks the isospin and rotational symmetries of the two-flavor NJL model, giving $SU_V(2) \times SU_A(2) \times SO(3) \times R^3 \to U_V(1) \times U_A(1) \times SO(2) \times R^3$. The condensate then spontaneously breaks chiral and translational symmetry according to $U_V(1) \times U_A(1) \times SO(2) \times R^3 \to U_V(1) \times SO(2) \times R^2$. The associated Goldstone modes are pions and phonons, the thermal fluctuations of which will be examined in Section 5.

By expanding Equation (1) about Equation (2), one can obtain the mean-field Lagrangian

$$\mathcal{L}_{\rm MF} = \bar{\psi}(i\gamma^\mu D_\mu + \gamma^0\mu - me^{i\gamma^5\tau^3 2bz})\psi - \frac{m^2}{4G}. \tag{3}$$

To find the free energy, it is convenient to remove the spatial dependence from the third term by performing a local chiral transformation $\psi \to e^{i\gamma^5\tau^3 bz}\psi$, which gives

$$\mathcal{L}'_{\rm MF} = \bar{\psi}(i\gamma^\mu D_\mu + \gamma^0\mu - m + \gamma^3\gamma^5\tau^3 b)\psi - \frac{m^2}{4G}. \tag{4}$$

The mean-field free energy is then given by

$$\Omega = -\frac{T}{V}\ln\int D\psi^\dagger D\psi\, e^{\int_0^\beta d\tau\int_V d^3x\,\mathcal{L}'_{\rm MF}} \tag{5}$$

$$= \frac{m^2}{4G} - \frac{T}{V}\,\mathrm{Tr}\ln(i\partial_0+\mu-H_D), \tag{6}$$

$$H_D = \gamma^0\gamma^j(-iD_j) + \gamma^0 m - \gamma^0\gamma^3\gamma^5\tau^3 b, \tag{7}$$

where V is a characteristic 3-volume element and the functional trace in Equation (6) includes color, flavor, and spinor degrees of freedom. The Dirac Hamiltonian H_D can be diagonalized exactly; see Refs. [32,33] for details. One can then evaluate the trace in Equation (6) and perform the Matsubara sum, giving the preliminary expression

$$\Omega_{\text{pre-reg}} = \frac{m^2}{4G} - \sum_f \frac{1}{2}\frac{N_c|e_fB|}{(2\pi)^2}\sum_{\ell\epsilon\xi}\int_{-\infty}^{+\infty} dk\left[|E-\mu| + \frac{2}{\beta}\ln\left(1+e^{-\beta|E-\mu|}\right)\right], \tag{8}$$

where we have written E instead of $E^\ell_{\xi,\epsilon}$ to lighten the notation. We have used the subscript "pre-reg" to indicate that this expression is formally infinite and must be regularized to obtain a well-defined theory. We present the final result below and then discuss the two regularization procedures involved in the calculation. We find

$$\Omega = \frac{m^2}{4G} + \sum_f\left(\Omega^f_{\rm vac} + \Omega^f_{\rm anom} + \Omega^f_\mu + \Omega^f_T\right) \tag{9}$$

$$\Omega^f_{\rm vac} = \frac{1}{4\sqrt{\pi}}\frac{N_c|e_fB|}{(2\pi)^2}\int dk\sum_{\ell\xi\epsilon}\int_{1/\Lambda^2}^\infty \frac{ds}{s^{3/2}}e^{-sE^2} \tag{10}$$

$$\Omega^f_{\rm anom} = -\frac{N_c|e_fB|}{(2\pi)^2}2b\mu \tag{11}$$

$$\Omega^f_\mu = -\frac{1}{2}\frac{N_c|e_fB|}{(2\pi)^2}\lim_{c\to\infty}\int_{-c}^{+c} dk\sum_{\ell\xi\epsilon}\left(|E-\mu|-|E|\right) \tag{12}$$

$$\Omega^f_T = -\frac{1}{2}\frac{N_c|e_fB|}{(2\pi)^2}\int dk\sum_{\ell\xi\epsilon}\frac{2}{\beta}\ln\left(1+e^{-\beta|E-\mu|}\right), \tag{13}$$

where

$$E^0 = \epsilon\sqrt{m^2+k^2}+b \qquad \epsilon=\pm1,\quad \ell=0 \tag{14}$$

$$E^\ell = \epsilon\sqrt{\left(\xi\sqrt{m^2+k^2}+b\right)^2+2|e_fB|\ell} \qquad \epsilon,\xi=\pm1,\quad \ell=1,2,3,\ldots, \tag{15}$$

and again we write E instead of $E^\ell_{\xi,\epsilon}$ in (10)–(13).

Following Refs. [13,32], we have adopted Schwinger proper-time regularization [34] to eliminate a UV divergence in the vacuum term in Equation (10). Due to the non-renormalizable nature of four-fermion interactions, the NJL model is sensitive to the choice of regularization method [30]. When studying inhomogeneous condensates, one must be especially careful with the choice of regularization method: a simple momentum cutoff leads to artifacts due to non-conservation of quark momenta scattering off the condensate [5], so a covariant scheme such as the proper-time method must be adopted. A detailed derivation of the regularization appearing in Equation (10) can be found in Appendix A of Ref. [13]. The basic idea is to extend the identity $|E|^{-2n} = \frac{1}{\Gamma(n)}\int_0^\infty ds\, s^{n-1}e^{-s|E|^2}$ to the value $n=-\frac{1}{2}$; the integral is divergent in this case, so we introduce the UV cutoff Λ by taking $\int_0^\infty \to \int_{1/\Lambda^2}^\infty$.

Second, the contribution from the quark medium in Equation (12) involves a difference of divergent quantities and must be treated carefully. The higher Landau levels (HLL) ($\ell > 0$) are insensitive to the type of cutoff used, i.e., a momentum cutoff $\theta(\Lambda' - |k|)$ vs. an energy cutoff $\theta(\Lambda' - |E|)$; either way, the expression is finite and identical in the limit $\Lambda' \to \infty$. The same does not hold, however, for the lowest Landau level ($\ell = 0$). As first shown in Ref. [32], before introducing the anomalous term, the integral in Equation (12) must be regularized by a large-energy cutoff $\theta(\Lambda' - |E|)$ to ensure that Ω is independent of b when $m = 0$. That integral can be manipulated into the form given by Equation (12) plus the anomalous term given by Equation (11). The details of this calculation reveal that the anomalous term originates from the spectral asymmetry of the LLL; it is also possible to derive this term from purely topological considerations [28].

We emphasize that the regularization discussed above is of a different character from the vacuum regularization. The latter arises due to the nonrenormalizability of the NJL model, and as such, Λ is introduced as a large but finite regulator that is never taken to infinity. The regularization of the medium term, however, involves cutoffs that are eventually taken to infinity (Λ' or c, depending on whether the anomalous term has been separated out). This regularization is necessary for consistency of the theory and originates from the asymmetry of the LLL. Finally, we note in passing that the medium term Ω_μ^f can be re-expressed by more explicit formulas for the LLL and HLL cases [27,33], which are useful for explicit calculations, although we omit them here.

Given the exact thermodynamic potential, it is possible in principle to determine the ground state, i.e., to compute the order parameters m and b that minimize the free energy, at any fixed μ, T, and B. In practice, computation of the Landau sums becomes more expensive with decreasing B and with increasing μ and T; for these parameter values, it is often more convenient to use a GL expansion. Moreover, as we discuss in Section 5, the GL expansion is crucial for analyzing the thermal fluctuations. In the next section, we introduce the GL expansion and examine its structure.

3. Ginzburg–Landau Expansion

GL theory is based on an expansion of a system's free energy near a phase transition in powers of an order parameter. For spatially inhomogeneous phases, one also expands about the gradient of the order parameter, including all terms that respect the global symmetries of the theory. The latter expansion—often dubbed a generalized GL expansion, although we will still use the term GL expansion in this paper—takes the following form at sixth order for the MDCDW phase:

$$\begin{aligned}\Omega^{(6)} = {} & \Omega_0 + \alpha_{2,0}|M|^2 - i\frac{\beta_{3,1}}{4}[M^*(\hat{B}\cdot\nabla M) - (\hat{B}\cdot\nabla M^*)M] + \alpha_{4,0}|M|^4 + \frac{\alpha_{4,2}}{4}|\nabla M|^2 \\ & - i\frac{\beta_{5,1}}{4}|M|^2[M^*(\hat{B}\cdot\nabla M) - (\hat{B}\cdot\nabla M^*)M] \\ & + i\frac{\beta_{5,3}}{16}[(\nabla^2 M^*)\hat{B}\cdot\nabla M - \hat{B}\cdot\nabla M^*(\nabla^2 M)] \\ & + \alpha_{6,0}|M|^6 + \frac{\alpha_{6,2}}{4}|M|^2|\nabla M|^2 + \frac{\alpha_{6,4}}{16}|\nabla^2 M|^2. \end{aligned} \tag{16}$$

This expansion includes all terms that can be formed from the available structures M, ∇M, and $\hat{B}$ that respect the broken symmetry group $U_V(1) \times U_A(1) \times SO(2) \times \mathbb{R}^3$, which characterizes the system after the formation of MDCDW. The coefficients $\alpha_{i,j}$ and $\beta_{i,j}$ are defined so that i counts the total powers of M and ∇M in a given term, while j counts only powers of ∇M. We use the notation $\beta_{i,j}$ instead of $\alpha_{i,j}$ for terms with an odd power of ∇M. Since ∇M is a vector while Ω is a scalar, these odd terms can only exist in a system where $SO(3)$ symmetry is explicitly broken and some other distinguished vector quantity

is present; in our case, this vector structure is provided by the magnetic field $\hat{B}$. In fact, the presence of $\hat{B}$ is necessary, but not sufficient, to avoid the vanishing of these odd terms, as we discuss below.

Substituting the ansatz $M(x) = e^{i2bz}$ into Equation (16), we find

$$\begin{aligned}\Omega^{(6)} = \alpha_{0,0} + \alpha_{2,0}m^2 + \beta_{3,1}m^2 b + \alpha_{4,0}m^4 + \alpha_{4,2}m^2 b^2 + \beta_{5,1}m^4 b \\ + \beta_{5,3}m^2 b^3 + \alpha_{6,0}m^6 + \alpha_{6,2}m^4 b^2 + \alpha_{6,4}m^2 b^4.\end{aligned} \tag{17}$$

Note that the numerical pre-factors inserted in Equation (16) are chosen for convenience to simplify the form of Equation (17). The coefficients can now be found explicitly by taking derivatives of Ω. Note that the $\beta_{i,j}$ coefficients can only be nonzero if Ω has a component that is odd in b. Inspecting Equations (9)–(15), we see that the only odd contributions in b come from the anomalous term and from the LLL: The HLL modes of opposite spin projections [corresponding to $\xi = \pm 1$ in Equation (15)] are interchanged under $b \to -b$, leaving Ω unaffected. This is not the case for the LLL, however, due to their spectral asymmetry. Both of these odd contributions—the anomalous term and the spectral asymmetry of the LLL—have a topological origin, resulting from a combination of the magnetic field and the condensate background. Indeed, there exist inhomogeneous chiral condensates in a magnetic field that do not exhibit such asymmetry, such as the real kink crystal [26], and the $\beta_{i,j}$ coefficients vanish for such condensates. Thus, we can think of the $\beta_{i,j}$ coefficients of MDCDW as encoding topological information of the theory, as claimed above.

Remarkably, if one uses the Euler–Maclaurin (EM) formula to approximate Landau sums by integrals plus an asymptotic series of correction terms in $|eB|^p$, one can obtain an all-orders formula for the coefficients in Equations (16) and (17), which gives the $|eB|^p$ contribution to each coefficient in a simple, closed-form expression [33,35]. To obtain this formula, one notes that the terms of Equation (16) take the form $\gamma_{n_m+n_b} m^{n_m} b^{n_b}$, where γ denotes α or β according to whether n_b is even or odd, respectively. This coefficient is given by the formula

$$\gamma_{n_m+n_b,n_b} = \frac{1}{(n_m/2)!n_b!}\partial_b^{n_b}\Big|_{b=0}\partial_{m^2}^{n_m/2}\Big|_{m=0}\Omega. \tag{18}$$

Several steps are required in order to systematically evaluate the derivatives in Equation (18). Here, we only offer a rough sketch of the main ideas behind the calculation, and we refer the reader to Refs. [33,35] for further details. The key is to recognize that Ω can be expressed in the form $\Omega = m^2/(4G) + \int_{-\infty}^{\infty} dk \Big[f(\sqrt{m^2+k^2}+b) + f(-\sqrt{m^2+k^2}+b) \Big]$ for a certain well-behaved function f. This enables one to take the derivatives in Equation (18) under the integral sign and then make repeated use of identities such as $\partial_{m^2} f\left(\pm\sqrt{k^2+m^2}+b\right) = \frac{1}{2k}\partial_k f\left(\pm\sqrt{k^2+m^2}+b\right)$ and $\partial_b f(\pm k + b) = \pm\partial_k f(\pm k + b)$, followed by several integrations by parts in k. This procedure enables one to arrive at formulas expressing the general coefficient $\gamma_{n_m+n_b,n_b}$ in terms of an integral expression of the form $\int_{-\infty}^{\infty} dk \frac{1}{k}\partial_k^{n_m+n_b-1} f(k)$, and these integrals turn out to be solvable analytically. Here, we have glossed over some important details such as the necessary separation of α and β cases as well as LLL and HLL contributions (with the EM formula being applied to the latter).

Working in units where $\Lambda = 1$, the formula resulting from the above calculation is given by

$$\alpha_{n_m+n_b,n_b} \sim \frac{\delta_{2,n}}{4G} + \frac{1}{(n_m/2)!n_b!}\sum_{f=u,d}\sum_{p=0,2,4,\ldots}^{\infty}\bar{\gamma}^{f,(p)}_{n_m+n_b,n_b} \tag{19}$$

$$\beta_{n_m+n_b,n_b} = \frac{1}{(n_m/2)!n_b!}\sum_{f=u,d}\bar{\gamma}^{f,(1)}_{n_m+n_b,n_b} \tag{20}$$

$$\bar{\gamma}^{f,(p)}_{n_m+n_b,n_b} = \begin{cases} \dfrac{N_c}{(2\pi)^2}\left[\dfrac{1}{4}-\dfrac{1}{3}\left(\mu^4+2\pi^2\mu^2T^2+\dfrac{7}{15}\pi^4T^4\right)\right], & \begin{matrix} n_m=0 \\ n_b=p=0 \end{matrix} \\ \dfrac{N_c}{(2\pi)^2}\left(-\dfrac{1}{2}+\mu^2+\dfrac{1}{3}\pi^2T^2\right), & \begin{matrix} n_m=2 \\ n_b=p=0 \end{matrix} \\ \dfrac{N_c|e_fB|^p}{(2\pi)^2}\dfrac{B_p^-}{p!}\dfrac{2^{1-(n_m/2)}}{(n_m-2)!!}\dfrac{(n-2)!!}{(n+2p-4)!!}I_{n+2p-4}, & \text{otherwise,} \end{cases} \tag{21}$$

where $n = n_m + n_b$ and

$$I_s^{(T=0)} = \begin{cases} -\gamma - 2\ln(2\mu), & s=0 \\ \mathrm{Re}\left[\left(i\sqrt{2}\right)^{s+2}(s-2)!! + \dfrac{2(s-1)!}{\mu^s}\right], & s=1,2,3,\ldots \end{cases} \tag{22}$$

$$I_s^{(T>0)} = \begin{cases} -\gamma + 2\ln\left(\dfrac{\beta}{4\pi}\right) - 2\,\mathrm{Re}\,\psi\left(\dfrac{1}{2}+i\dfrac{\beta\mu}{2\pi}\right), & s=0 \\ \mathrm{Re}\left[\left(i\sqrt{2}\right)^{s+2}(s-2)!! - 2\left(-\dfrac{i\beta}{2\pi}\right)^s\psi^{(s)}\left(\dfrac{1}{2}+i\dfrac{\beta\mu}{2\pi}\right)\right], & s=1,2,3,\ldots. \end{cases} \tag{23}$$

Here, B_p^- denotes the pth Bernoulli number, with the convention $B_1^- = -\frac{1}{2}$, and $\psi^{(s)}$ is the sth polygamma function. In the case $n_m = n_b = 0$ and $p > 0$, the expression for $\bar{\gamma}^{f,(p)}_{0,0}$ contains the formal ratio $(-2)!!/(-2)!!$, which should be interpreted as 1.

The generalization of Equation (17) to Nth order is

$$\Omega^{(N)} = \alpha_{0,0} + \sum_{n=2}^{N}\sum_{n_b\in S_n}\gamma_{n,n_b}m^{n-n_b}b^{n_b}, \tag{24}$$

where

$$S_n = \begin{cases} 0,2,\ldots,n-2, & n \text{ even} \\ 1,3,\ldots,n-2, & n \text{ odd}, \end{cases} \tag{25}$$

and $\gamma_{i,j}$ denotes $\alpha_{i,j}$ or $\beta_{i,j}$ according to whether n_b is even or odd, respectively. With Equations (19)–(25) at hand, it is easy to compute many properties of MDCDW at finite temperature and density, such as the ground-state order parameters and critical temperature, the equation of state, and even the effect of thermal phonon fluctuations beyond mean field theory. However, it was found in Refs. [35,36] that the sixth-order expansion is not very accurate, and that reliable results require increasing to order $N \gtrsim 20$. The reliance on such large orders raises questions about the convergence properties of the GL expansion: Where in parameter space can the expansion be trusted, and up to what order? The urgency of this question is heightened by the moderate to large values of m and b that appear in key regions of parameter space. Typically, a GL expansion is unreliable in regions where the expansion parameters are too large compared to some characteristic scale of the system. Thus, the apparent agreement between our results as computed directly from Ω and those computed from the GL expansion may seem puzzling.

In order to address the above concerns, we can start by asking with respect to what characteristic scale of the system the expansion takes place. There are several dimensionful parameters of the model that could potentially set the scale for the validity of the GL

expansion: We have μ, T, Λ, and $\sqrt{eB}$, which all have dimension one. To see which of these parameters controls the convergence of the GL expansion on a heuristic level, we can look to the coefficient functions given above and note that a factor of μ^s appears in the denominator of Equation (22). By dimensional analysis, there is also a suppressed power of Λ^s appearing in the denominator of the other term in the same formula. As the total order n of a GL coefficient increases, it introduces higher powers of μ and Λ in its denominator, which may control the higher powers of m and b multiplying that coefficient. Thus, one might expect the expansion to be well behaved when $m, b < \mu$. As a first step toward making this claim precise, in Ref. [37], the radius of convergence in m was calculated for the simpler case of a homogeneous condensate without a magnetic field, i.e., $b = B = 0$: It was found that the series converges for $|m| < \sqrt{\mu^2 + (\pi T)^2}$. In Section 6 of the present paper, we extend this result, showing that in the general case of $b, B > 0$, the GL expansion in Equation (24) at any fixed EM order $|eB|^p$ converges when $|m| + |b| < \sqrt{\mu^2 + (\pi T)^2}$.

Let us also stress that there are two senses in which one may ask about the accuracy of the GL expansion. First, there is the extent to which the expansion [e.g., in the form of (16) or higher-order truncations] approximates the free energy given by Equations (9)–(13). This is a mathematical question that can be studied rigorously. While there are some subtleties concerning the Euler–Maclaurin formula, the answer is essentially given by the radius of convergence calculated in Section 6: When $|m| + |b| < \sqrt{\mu^2 + (\pi T)^2}$, the GL expansion at a fixed EM order $|eB|^p$ converges, and hence the mean-field free energy is well approximated by a sufficiently high-order expansion. This conclusion is clearly visible from the numerical results shown in the next section, which plot comparisons of Ω as computed from the exact formula and from GL expansions of various orders.

The second question is whether mean-field theory provides an accurate description of the condensate, or whether the effects of fluctuations are significant. This issue is more subtle, since several different kinds of fluctuations may contribute, including thermal phonon fluctuations, charged-pion fluctuations, and quantum fluctuations of the condensate. A complete treatment of all such effects lies beyond the scope of the present work. However, thermal phonon fluctuations are studied in detail in Section 5, where we show that the condensate avoids the LP instability that affects analogous single-modulated phases in the absence of a magnetic field.

4. Ground State Solutions and Critical Temperature

4.1. DCDW Phase ($B = 0$)

To place our results in context, we begin by considering the DCDW condensate, i.e., the $B \to 0$ limit of MDCDW. The free energy for this phase is given by the $B \to 0$ limit of Equations (9)–(13), which can be obtained by applying the EM formula to the Landau sums. The GL expansion in Equation (17) with coefficients given by Equations (19)–(23) still correctly describes the DCDW phase: In particular, the $\beta_{i,j}$ coefficients are linear in B and hence vanish when $B = 0$, and the EM series in the α coefficients reduces to a single term.

We perform our calculations in the chiral limit, in which the bare quark masses vanish. We use parameter values $\Lambda \approx 636.79$ and $G = 6/\Lambda^2$, which are chosen to fix the vacuum effective quark mass at $m_{\text{vac}} = 300$ MeV and pion decay constant at its chiral limit value of $f_\pi = 88$ MeV. These (and very similar) choices of f_π and M_{vac} are common in the literature for studying the phase diagram in the NJL model [13,14,31,32,35]. As discussed by Nickel in Ref. [14], tuning the NJL parameters in proper-time regularization to reproduce all vacuum observables while simultaneously yielding a phenomenologically acceptable phase diagram is a nontrivial task. The values adopted here correspond to a condensate magnitude of $|\langle\bar{\psi}\psi\rangle|^{1/3} = 172$ MeV, which falls somewhat short of the commonly quoted phenomenological range of approximately 200–260 MeV [29]. Retuning the parameters

to increase $|\langle\bar{\psi}\psi\rangle|$ would lead to a value of $M_{\rm vac}$ that is too small to reproduce a phase diagram phenomenologically consistent with that of similar models. The typical choice of $M_{\rm vac} = 300$ MeV, therefore, is ultimately motivated not only by the goal of reproducing all vacuum observables, but also the basic phase diagram and phenomenology expected from QCD.

The ground state solutions are shown in Figure 1. In the top-left panel, the values of m (solid) and b (dashed) that minimize the free energy are plotted across a wide range of chemical potentials, $0 < \mu < 600$ MeV (the high end of this range pushes the limit of where the model can be trusted, since we use a high-energy regulator of $\Lambda \approx 637$ MeV). This range of chemical potentials naturally separates into four regions: For $0 < \mu < 311$ MeV, we have a homogeneous, chirally broken phase with $m \approx 300$ MeV. For 311 MeV $< \mu <$ 341 MeV, we have an inhomogeneous phase, where both chiral and translational symmetries are broken. In this region, m decreases and b increases with μ. The condensate then vanishes, giving a chirally restored phase for 341 MeV $< \mu <$ 491 MeV, and finally, an inhomogeneous phase returns for $\mu >$ 491 MeV.

The top-left panel also demonstrates that a high-order GL expansion is very accurate over a certain range of parameter space. The data computed from the exact free energy are plotted with black lines, while red lines show data computed with a 30th-order GL expansion. The GL data are not accurate over the entire region, with significant divergence from the correct results for small values of μ. Notably, however, the entire inhomogeneous region at intermediate μ falls under the green shaded zone, which indicates where $m + b < \mu$. As we prove in Section 6, the expansion converges in this region, which explains the accuracy of these results. The top-right panel zooms in on the first inhomogeneous region and shows GL approximations at various orders. It is clear that the expansion improves with increasing order over this region, with sixth-order being quite crude and 30th-order being indistinguishable from the exact results.

In the bottom-left panel of Figure 1, we plot the order parameters for $T = 20$ and 40 MeV. We see that T disfavors the condensate, suppressing m at fixed μ. The $T > 0$ data for this panel are computed using a 30th-order GL expansion, and the edge of the GL convergence regions for each T are indicated with vertical lines. The convergence region expands at larger T, as both the decrease in m and the increase in T allow the convergence condition $m + b < \sqrt{\mu^2 + (\pi T)^2}$ to be satisfied for smaller μ. In the bottom-right panel, we plot the phase diagram of DCDW in the μ-T plane for $\mu < 400$ MeV. The black curve is the critical temperature T_c, which is defined where m vanishes in a second-order transition and chiral symmetry is restored. The gray shaded region shows where inhomogeneity is favored, and the green shaded region shows where the GL expansion converges. The convergence region notably covers the entire inhomogeneous part of the phase diagram.

Let us highlight how the GL expansion enables simpler calculations of the data presented in Figure 1. To find the order parameters from the exact free energy, one must search for the minimum of Equations (9)–(13). Computing these quantities requires numerical integration, which becomes more expensive when $T > 0$ and even more so at $B > 0$. On the other hand, solving the corresponding GL stationary equations amounts only to solving a pair of polynomial equations in m and b. The simplification is especially dramatic when computing critical temperature shown in the bottom-right panel. Rather than solving for the ground state across the entire μ-T plane, we note that m vanishes precisely when the minimum value of $\partial\Omega/\partial(m^2)|_{m=0}$ vanishes, i.e., when the following two conditions are met:

$$\left.\frac{\partial\Omega}{\partial(m^2)}\right|_{m=0} = 0 \tag{26}$$

$$\frac{\partial}{\partial(b^2)}\left(\left.\frac{\partial\Omega}{\partial(m^2)}\right|_{m=0}\right) = 0. \tag{27}$$

At fixed μ, one can search for the values of b and T that solve Equations (26) and (27), which again are just polynomials (with T-dependent coefficients that are inexpensive to compute) when using the GL expansion. For the homogeneous region where $b = 0$, these reduce even further to $\alpha_{2,0} = 0$. Using the explicit expression for $\alpha_{2,0}$ given by Equations (19)–(21), we find that the critical temperature on the left side of the blue dot in the bottom-right panel of Figure 1 is given by $T_c/\Lambda = \sqrt{\frac{3}{\pi^2}\left[\frac{1}{2} - (\mu/\Lambda)^2\right] - \frac{1}{12}}$.

Before moving to the $B > 0$ case, it is worth highlighting that already at $B = 0$, the behavior of the condensate as a function of μ is nontrivial. After the first-order transition at $\mu = 311$ MeV, as μ increases, the condensate magnitude decreases, then vanishes over an intermediate range, then returns and rises again to large values. It is interesting to consider the physical origin of such behavior: In Ref. [35], it was proposed that these features might result from a competition between the pairing mechanisms that give rise to the condensate. In Section 2, we mentioned that with increasing μ, the quark–antiquark pairs (which give rise to the homogeneous condensate in vacuum) are suppressed, while quark–hole pairs (which have net momentum and thus lead to inhomogeneity) are enhanced due to the formation of a large Fermi surface. Because these two effects compete, it is plausible that at lower values of μ the former effect (suppression of quark–antiquark pairs) dominates, while at larger μ, the latter effect (enhancement of quark–hole pairs) dominates. Indeed, the Fermi surface expands without bound as μ increases, creating more phase space for quark–hole pairs to form, which suggests that eventually this effect should win out. This would also explain the large increase in b when the condensate returns at large μ, since quark–hole pairs forming at the Fermi surface have momenta of order μ. Nonetheless, we stress that this description is fairly heuristic and may be oversimplified; it would be interesting to investigate such a picture more rigorously in future work.

4.2. MDCDW Phase $(B > 0)$

Let us now introduce a magnetic field. Figure 2 shows four panels analogous to those of Figure 1 but computed at $B = 1.5 \times 10^{18}$ G. Several new features are worth commenting on. First, observe in the top-left panel that we have a small but nonvanishing $b > 0$ at all finite chemical potentials. This is a purely topological effect resulting from the anomalous term given by Equation (11): As this term is proportional to $-b\mu$, it clearly favors b whenever $\mu > 0$, whereas explicit expressions for the medium term in Equation (12) show that it vanishes in this region. Next, we see that the regions where the DCDW phase is inhomogeneous are enhanced for MDCDW, having larger m and occurring over a wider range of μ. Moreover, the intermediate region 341 MeV $< \mu <$ 491 MeV where DCDW vanishes is replaced by a smaller window 370 MeV $< \mu <$ 452 MeV for MDCDW in which m is small but nonvanishing. This feature, first pointed out in Ref. [35] and dubbed the "remnant mass," is a result of non-analytic points in Ω related to Landau discretization. One can show that $\partial\Omega/\partial(m^2)|_{m=0}$ must be negative near certain values of b, forcing the system to prefer $m > 0$ for any μ.

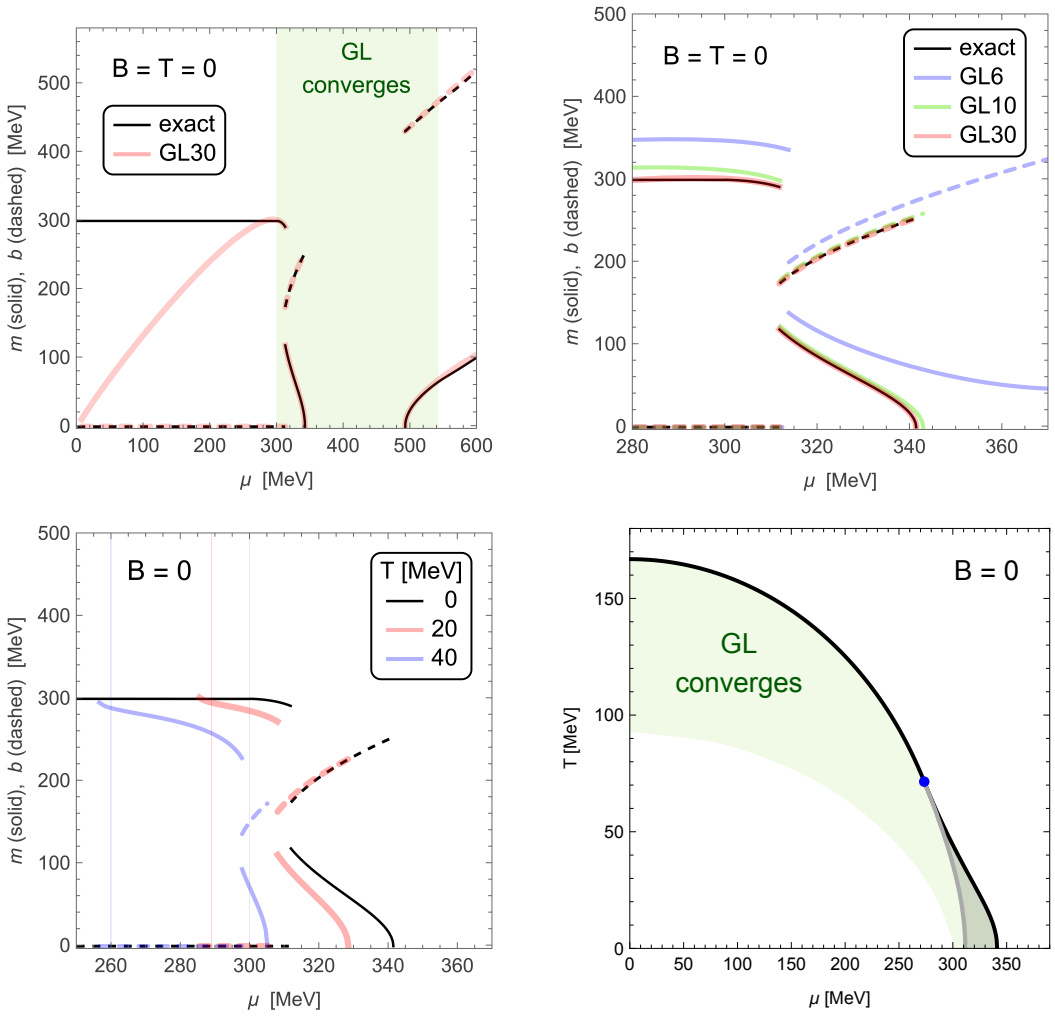


Figure 1. Ground state order parameters and phase diagrams of the DCDW phase ($B = 0$). In all panels except the (**bottom-right**), m is plotted with solid lines and b with dashed lines. (**Top**): Both upper panels show values of m and b that minimize the free energy at $T = 0$, computed using the exact free energy (black curves) and GL expansions of various orders (colored curves). The green region in the (**top-left**) panel indicates where $m + b < \mu$ and hence the GL expansion is reliable. (**Bottom Left**): m and b are plotted at three temperatures. Data for $T > 0$ are computed with a 30th-order GL expansion. The thin vertical lines indicate where $m = \mu$ for the corresponding temperature, which is the edge of the region where the GL expansion is reliable. (**Bottom Right)**: The black curve shows the critical temperature, i.e., where m vanishes and chiral symmetry is restored. The condensate is inhomogeneous in the gray shaded region, which is separated from the homogeneous phase by a first-order transition depicted by a gray line. The blue dot is a critical point where the first-order transition disappears; in the $B = 0$ case, this point occurs at the critical temperature (compare with the $B > 0$ case in Figure 2). The green shaded region (which encompasses the entire inhomogeneous region) indicates where $m + b < \sqrt{\mu^2 + (\pi T)^2}$, and hence the GL expansion converges in the ground state.

From the top panels, we again see that a high-order GL expansion is reliable in the region of interest. However, the magnetic field introduces some non-analytic behavior that is not captured by the GL expansion: The exact solutions for m (solid black line in the top-right panel of Figure 2) contain small kinks and weakly first-order jumps, whereas the 30th-order GL expansion gives a smoothed approximation of these data. The remnant mass is another non-analytic feature that the GL expansion does not capture. The reason for these discrepancies is not intrinsic to the GL expansion, but arises due to the use of the EM formula to derive the expressions for the GL coefficients. The non-analytic features in Ω are related to Landau discretization, and the EM formula eliminates this non-analyticity by

approximating the sums as integrals. Even the higher-order terms in the EM formula do not re-introduce the original non-analytic features in the free energy; we return to some further discussion of this topic in Section 6.3. For now, we only note that (1) at the magnetic fields considered here, the GL expansion still provides a good approximation to the exact data, while smoothing out certain pathologies, and (2) above small temperatures of $T \simeq 5$ MeV, these pathologies are essentially erased and the GL results again agree almost perfectly with the exact solutions.

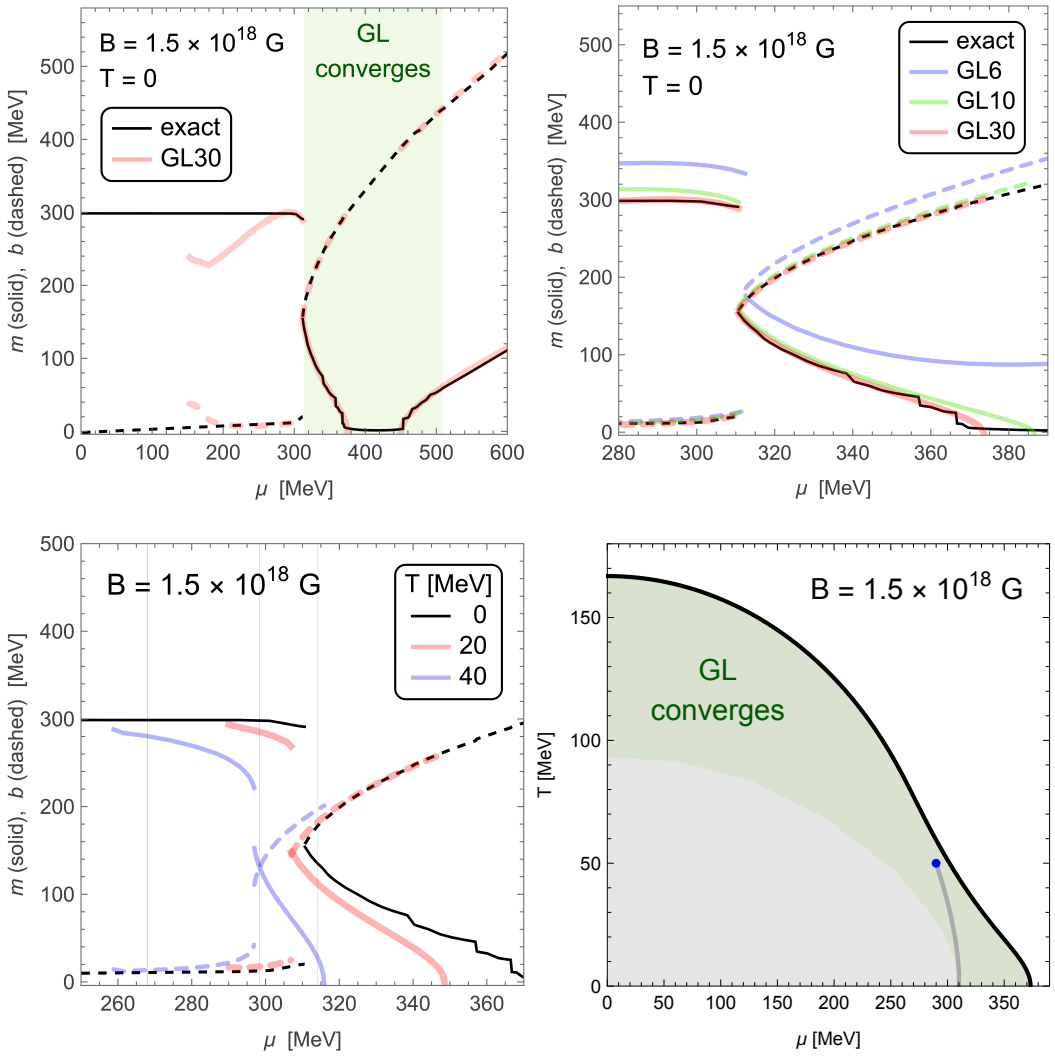


Figure 2. Ground state order parameters and phase diagrams of the MDCDW phase at $B = 1.5 \times 10^{18}$ G. In all panels except the (**bottom-right**), m is plotted with solid lines and b with dashed lines. Each panel here is the analogous version at 1.5×10^{18} G of the corresponding panel in Figure 1. Key differences between the two panel sets are discussed in the text.

The bottom-right panel of Figure 2 shows the phase diagram of MDCDW for $\mu < 400$ MeV. Because m has increased over the region 311 MeV $< \mu <$ 370 MeV compared to DCDW, so too has the critical temperature. Moreover, the entire region under the black curve corresponds to an inhomogeneous phase (apart from the line $\mu = 0$), hence this entire section is shaded gray. The gray line now only demarcates a first-order jump between large and small b, rather than a genuine phase transition. Again the gray line terminates in a critical point (indicated by a blue dot); at temperatures above this point, there is no first-order jump in order parameters with increasing μ. At $B > 0$, this critical point occurs below the T_c curve, so any two points below the black curve can be connected by a path along which the order parameters vary continuously. Again we show where the

GL expansion converges (green shaded region), based on whether the ground state order parameters satisfy $m + b < \sqrt{\mu^2 + (\pi T)^2}$, and we note that this parameter space includes the region of interest.[1] The small remnant mass at $\mu \gtrsim 370$ MeV also gives rise to a small "remnant critical temperature" over the same region. This feature is not indicated in the bottom-right panel of Figure 2, which was computed using a GL expansion and hence does not capture the remnant mass phenomenon. However, it is possible to approximate the remnant T_c using other methods, as described in Ref. [35].

In Figure 3, we plot the order parameters and critical temperature for several magnetic field values. Both plots show that magnetic fields on the order of 10^{18} G significantly strengthen the condensate, increasing m and widening the range of chemical potentials where m is large. For $B \gtrsim 2 \times 10^{18}$ G, the two regions of large m merge, and the condensate becomes strongly favored for all chemical potentials. For smaller fields, the condensate is still technically favored at all μ due to the remnant mass effect described above, although the size of the remnant mass is exponentially suppressed for $B \ll 10^{18}$ G. The remnant mass is not detected by the GL expansion, and we omit it from the plots in Figure 3, which are generated entirely using a 30th-order GL expansion. We also note in passing that at $\mu = 0$, our numerical results exhibit a very slight increase of T_c with magnetic field (∼0.1% difference between $B = 0$ and $B = 5 \times 10^{18}$ G), which is too small to notice visually. This order of magnitude increase is consistent with what would be expected from the results in Ref. [32], which analyzed the same model without the use of a GL expansion; that study did not consider $T > 0$, but at $T = 0$, they found that an increase of m with B at $\mu = 0$ (magnetic catalysis) does not become noticeable until magnetic fields reaching a few times 10^{19} G.

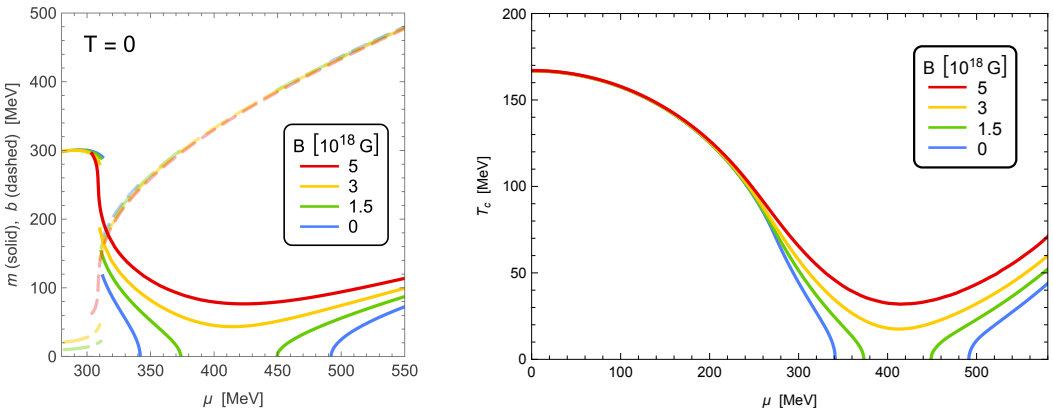


Figure 3. Order parameters (**left panel**) and critical temperature (**right panel**) of MDCDW at various magnetic fields from 0–5 × 10^{18} G. All data are computed with a 30th-order GL expansion. Small but nonzero "remnant" values of m and T_c at intermediate μ for 1.5 × 10^{18} G are not captured by the GL expansion; thus, the curves vanish over this region, even though in principle $T_c > 0$ everywhere. The (**right panel**) is adapted from Figure 4 of Ref. [35].

We claim the increase in m and T_c with stronger magnetic fields, as shown in Figure 3, is not merely a magnetic effect, but a topological one. With the GL expansion at hand, it is easy to verify this claim. Recall that the $\beta_{i,j}$ coefficients encode topological information about MDCDW, since their only contribution comes from the asymmetry of the LLL. Thus, it is illuminating to analyze the phase in a strong magnetic field but using a GL expansion where the $\beta_{i,j}$ coefficients have been removed by hand. In principle, this need not eliminate the effect of the magnetic field, since B still enters into the higher-order EM terms in the α coefficients. Nevertheless, Figure 4 shows that MDCDW without the $\beta_{i,j}$ coefficients is indistinguishable from the DCDW phase (in which $B = 0$).

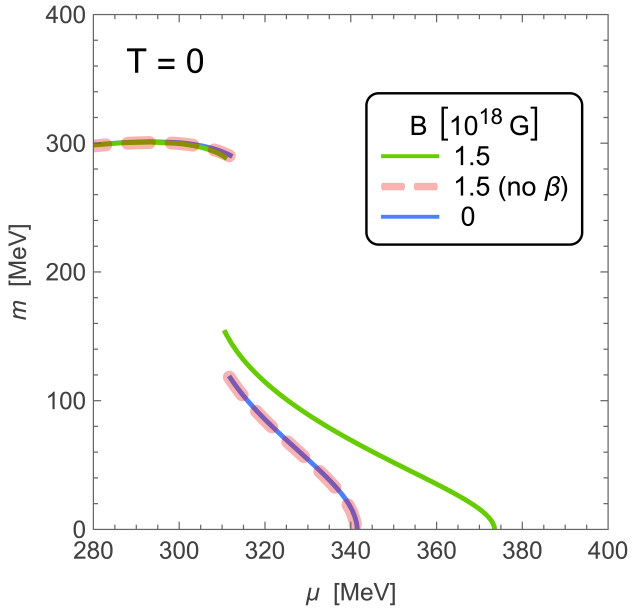


Figure 4. The order parameter m for MDCDW with a magnetic field of 1.5×10^{18} G, calculated using a GL expansion that includes the $\beta_{i,j}$ coefficients (green curve) and one that does not include the $\beta_{i,j}$ coefficients (red dotted curve). The latter is indistinguishable from the same curve for the DCDW phase, where $B = 0$ (blue curve).

The temperatures in the right panel of Figure 3 are very large compared to those of cold neutron stars, which typically fall on the order of several keV. Thus, in this model, MDCDW can exist at cold NS temperatures for any densities and magnetic fields where the T_c curves in Figure 3 do not vanish. For fields $\gtrsim 2 \times 10^{18}$ G, the phase is preferred at all densities; for 1.5×10^{18} G, it is favored up to $\mu = 373$ MeV, corresponding to $\approx 2.85\ n_s$, where $n_s = 0.16$ fm^{-3} denotes nuclear saturation density. All smaller magnetic field values fall between the blue and green curves in Figure 3, and hence are favored up to at least $\mu = 342$, corresponding to $\approx 2.2\ n_s$. These estimates do not take the remnant critical temperature into account, which has the potential to extend the range of viable densities at these smaller field strengths.

Another intriguing aspect of the T_c curves in Figure 3 is the larger temperatures at which MDCDW is favored for fields $\gtrsim 3 \times 10^{18}$ G. These temperatures reach several times 10 MeV, which is the temperature scale relevant to the remnants formed after a binary neutron star merger. Simulations using full general relativistic magnetohydrodynamics have found densities up to 6 n_s in such objects [38], which corresponds to the start of the high range of chemical potentials ($450\ \text{MeV} < \mu < 500\ \text{MeV}$) in Figure 3 where m and T_c begin to increase. Similar studies have found that the magnetic fields of such objects can be enhanced by several orders of magnitude due to various magnetic instabilities [39–41]. If magnetic fields in the cores of such objects can reach the scale of 10^{18} G, then this opens the door for inhomogeneous condensates such as MDCDW to become viable.

While we have been analyzing the mean field theory of MDCDW, there remains the question of its thermal stability beyond mean field theory. We address this topic in the next section.

5. Thermal Stability

When moving beyond mean field theory, many single-modulated inhomogeneous phases are subject to the LP instability [22–25], which erases the long-range order at any finite temperature. In the setting of dense QCD, this instability has been found, for example, in the periodic real kink crystal [26], DCDW [42], and quarkyonic phases [43]. In this section,

we review the theory of this instability, and then show that it is avoided by MDCDW due to the topological $\beta_{i,j}$ terms in its GL expansion. We also show results on the threshold temperature, which is where thermal phonon fluctuations begin to significantly affect the long-range order of the condensate.

The formation of a single-modulated inhomogeneous phase spontaneously breaks translational symmetry along the modulation direction, giving rise to phonons as Nambu–Goldstone modes. The LP instability occurs when the spectrum of these phonons contains soft modes in the transverse direction, meaning the dispersion is quadratic rather than linear in the transverse momentum. This quadratic dependence leads to an infrared (IR) divergence in the average square phonon fluctuation for any finite temperature, giving rise to the LP instability. The long-range order of the original phase is thus washed out by thermal fluctuations.

It was pointed out in Ref. [26] that the above argument does not necessarily apply to systems with an external vector field. Such a field introduces new structures in the GL expansion (as we have already seen for MDCDW), which can modify the low-energy theory and produce linear terms in the transverse modes of the phonon spectrum. Indeed, this was shown to be the case for a sixth-order expansion of MDCDW in Ref. [44], and for an arbitrary Nth-order expansion in Ref. [36]. Let us review these arguments.

Since the formation of MDCDW spontaneously breaks chiral and translational symmetries, both a neutral pion (τ) and phonon (u) arise as Goldstone modes. However, the form of the condensate $M(x) = me^{i2bz}$ gives rise to a locking mechanism between these modes,

$$M(x) \to e^{i\tau} m e^{i2b(z+u)} = e^{i(\tau+2bu)} M(x). \tag{28}$$

Thus, the modes are not independent, and we are free to analyze either the pion, the phonon, or a combination of the two; we choose the phonon.

Let us perturb the ground state $M_0(x) = m_0 e^{i2b_0 z}$ with a small phonon fluctuation $u(x) = u(x, y, z)$ and keep terms up to second order in u,

$$M(x) = M[z + u(x)] \tag{29}$$

$$\simeq M_0(z) + M_0'(z)u(x) + \tfrac{1}{2}M_0''(z)[u(x)]^2 + \cdots . \tag{30}$$

The free energy of the perturbed condensate can then be found by inserting Equation (30) into the GL expansion and keeping terms up to second order in u. For a sixth-order GL expansion, this takes the form

$$\mathcal{F}^{(6)}[u(x)] = \mathcal{F}_0^{(6)} + m^2 b^2 v_z^2 (\partial_z u)^2 + m^2 b^2 v_\perp^2 (\partial_\perp u)^2 + m^2 b^2 \zeta^2 (\partial_z^2 u + \partial_\perp^2 u)^2, \tag{31}$$

where $\mathcal{F}^{(6)}$ denotes the ground state free energy in mean field theory, and we use the notation $(\partial_\perp u)^2 = (\partial_x u)^2 + (\partial_y u)^2$ and $\partial_\perp^2 u = (\partial_x^2 u + \partial_y^2 u)$. The coefficients v_z^2, $v_\perp^2$, and ζ^2 are expressions involving GL coefficients that appear when bringing the perturbed expansion into the form of Equation (31),

$$v_z^2 = \alpha_{4,2} + 3b\beta_{5,3} + m^2\alpha_{6,2} + 6b^2\alpha_{6,4} \tag{32}$$

$$v_\perp^2 = \alpha_{4,2} + b\beta_{5,3} + m^2\alpha_{6,2} + 2b^2\alpha_{6,4} \tag{33}$$

$$\zeta^2 = \tfrac{1}{4}\alpha_{6,4}. \tag{34}$$

To reduce clutter, we use m and b to denote the ground state values m_0 and b_0. It must be understood, however, that the condensate has been perturbed about the ground state, and hence m and b satisfy the stationary equations. At sixth order, one of these equations takes the form

$$0 = \frac{\partial \Omega^{(6)}}{\partial b} = m^2 \left[2b(\alpha_{4,2} + m^2 \alpha_{6,2} + 2b^2 \alpha_{6,4}) + (\beta_{3,1} + m^2 \beta_{5,1} + 3b^2 \beta_{5,3}) \right], \tag{35}$$

and is responsible for the vanishing of a linear term $\partial_z u$ that appears when deriving Equation (31).

Defining $\theta(x) = mbu(x)$ for convenience, the Lagrangian corresponding to Equation (31) is given by

$$\mathcal{L}^{(6)} = (\partial_0 \theta)^2 - v_z^2 (\partial_z \theta)^2 - v_\perp^2 (\partial_\perp \theta)^2 - \zeta^2 (\partial_z^2 \theta + \partial_\perp^2 \theta)^2. \tag{36}$$

It follows that the spectrum of the fluctuation field is anisotropic and linear in both the longitudinal and transverse directions,

$$E \simeq \sqrt{v_z^2 k_z^2 + v_\perp^2 k_\perp^2}, \tag{37}$$

where $k_\perp^2 = k_x^2 + k_y^2$.

To see how the fluctuation affects the condensate average $\langle M \rangle$, we insert the ansatz $M_0(x) = me^{i2bz}$ into Equation (30) and take the average. Using the relation $\langle \cos(2bu) \rangle = e^{-2\langle b^2 u^2 \rangle}$, we find

$$\langle M \rangle = e^{-2\langle b^2 u^2 \rangle} M_0(x). \tag{38}$$

Using the path integral formula

$$\langle \cdots \rangle = \frac{\int \mathcal{D}u(x) \cdots e^{-S(u^2)}}{\int \mathcal{D}u(x) e^{-S(u^2)}} \tag{39}$$

to take the averages, where $S(u^2)$ is the finite-temperature effective action given by

$$S(u^2) = T \sum_n \int_{-\infty}^{\infty} \frac{d^3k}{(2\pi)^3} \left[\omega_n^2 + (v_z^2 k_z^2 + v_\perp^2 k_\perp^2 + \zeta^2 k^4) \right] m^2 b^2 u^2, \tag{40}$$

we find

$$\langle b^2 u^2 \rangle = \frac{T}{2(2\pi)^2} \sum_n \int_0^{\infty} dk_\perp k_\perp \int_{-\infty}^{+\infty} dk_z \frac{1}{m^2(\omega_n^2 + v_z^2 k_z^2 + v_\perp^2 k_\perp^2 + \zeta^2 k^4)}. \tag{41}$$

To understand why the LP instability typically occurs, consider the situation in which no magnetic field is present, and hence the $\beta_{i,j}$ coefficients all vanish. In that case, Equations (33) and (35) give

$$0 = m^2 2b v_\perp^2. \tag{42}$$

When the ground state is inhomogeneous, we have $m > 0$ and $b > 0$, so Equation (42) implies $v_\perp^2 = 0$. It follows that the IR contribution coming from the lowest Matsubara mode ($\omega_0 = 0$) of Equation (41) is divergent. Thus, $\langle b^2 m^2 \rangle$ diverges at any $T > 0$, and $\langle M \rangle$ vanishes by Equation (38), which signals the destruction of long-range order due to fluctuations.

For MDCDW, of course, the $\beta_{i,j}$ coefficients do not vanish. Because the dominant contribution to (41), which causes the LP instability in the $B = 0$ case, comes from the IR region and lowest Matsubara mode, we choose to focus only on the fluctuations coming from this region. Considering the ω_0 mode, the IR contribution to (41) can be estimated as

$$\langle b^2 u^2 \rangle \simeq \frac{T}{8\pi m |v_z v_\perp|}. \tag{43}$$

To study the effect of the fluctuations quantitatively, we define the threshold temperature $T_{\rm thr}$ as the temperature at which the exponent in Equation (38) equals -1, i.e., when $\langle b^2 m^2 \rangle = 1/2$. From Equation (43), we have[2]

$$T_{\rm thr} = 4\pi m |v_z v_\perp|. \tag{44}$$

At fixed μ, one can find the threshold temperature numerically by searching for values of m, b, and T that simultaneously satisfy Equation (44) and the two stationary equations. However, the velocities in Equations (32) and (33) are only calculated at sixth order; as we have seen, numerical results computed at sixth order are not very accurate. In Figure 5, we show the threshold temperature computed at various GL orders. The results clearly stabilize by 30th order and are not very accurate for low orders. Thus, we again use a 30th-order GL expansion for the remainder of the calculations in this section.

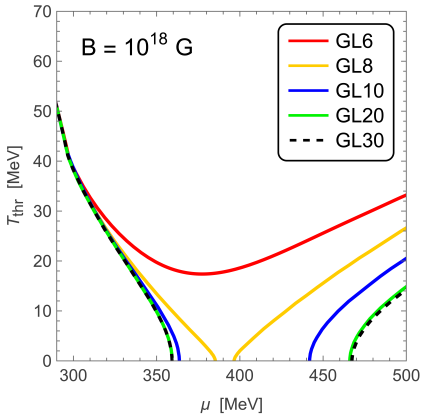


Figure 5. Threshold temperature at $B = 10^{18}$ G computed at various orders of the GL expansion. The lower-order expansions are not very accurate, but results stabilize by at least 30th order. This figure is adapted from Figure 1 of Ref. [36].

Deriving the higher-order formulas for the velocities would be highly cumbersome to do by hand: The 30th-order expansion contains 225 terms, each one containing many occurrences of M into which one must substitute the expression in Equation (30) before simplifying. Remarkably, this procedure can be avoided by writing out the general form of an Nth-order term in the GL expansion, inserting Equation (30), and applying a series of induction arguments [33,36]. In this approach, one can show that the vanishing of the linear term $\partial_z u$ in Equation (31) (due to the stationary equations) holds at every order, and one can obtain the following Nth-order velocity formulas,

$$v_z^2 = \sum_{n=2}^{N} \sum_{n_b \in S_n} \gamma_{n,n_b} m^{n-n_b-2} b^{n_b-2} \frac{n_b(n_b-1)}{2} \tag{45}$$

$$v_\perp^2 = \sum_{n=2}^{N} \sum_{n_b \in S_n} \gamma_{n,n_b} m^{n-n_b-2} b^{n_b-2} \left\lfloor \frac{n_b}{2} \right\rfloor, \tag{46}$$

where $\lfloor \cdot \rfloor$ is the floor function and γ_{n,n_b} and S_n are defined as in Equations (24) and (25).

Using Equations (45) and (46), we can readily compute the threshold temperature at 30th order for various magnetic fields. In Figure 6, we show the threshold temperature (dashed) and critical temperature (solid) of three large magnetic fields on the order of 10^{18} G. The key result is that $T_{\rm thr}$ is close to T_c, indicating that the condensate is stable for most of the parameter space where it is preferred in mean field theory.

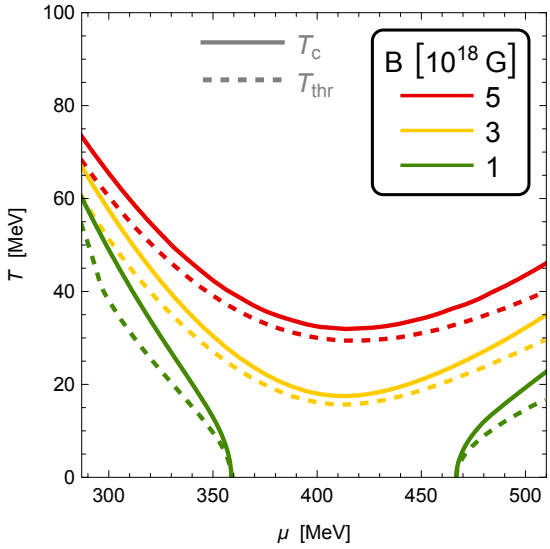


Figure 6. Threshold temperature (dashed) and critical temperature (solid) at $B = 1, 2$, and 3×10^{18} G. The threshold temperature is close to the critical temperature, indicating that MDCDW is stable against thermal fluctuations over a large region of parameter space. This figure is adapted from Figure 4 of Ref. [36].

In Figure 7, we plot $T_{\rm thr}$ and $T_{\rm c}$ at smaller magnetic fields. As B decreases, the fluctuations become more significant, as indicated by the vanishing ratio $T_{\rm thr}/T_{\rm c}$. Over the range of μ where inhomogeneity is favored at $B = 0$, the $T_{\rm c}$ curves approach that of the DCDW phase, while $T_{\rm thr}$ vanishes. The vanishing of $T_{\rm thr}$ in this limit is another manifestation of the LP instability. In Figure 8, we plot the same curves superposed on the phase diagram of DCDW. The threshold temperature never drops into the region of parameter space where DCDW is homogeneous, as there is no instability in that phase. Notice that even for the smallest field shown of 5×10^{16} G, the threshold temperature is on the order of several MeV over the range where large b is favored. Such temperatures are large compared to those of cold neutron stars, indicating that MDCDW could be thermally stable in such an environment.

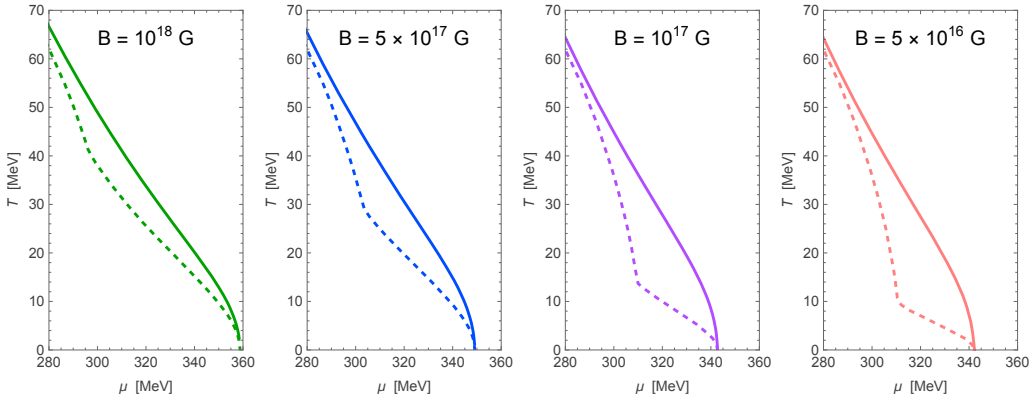


Figure 7. Critical temperature (solid) and threshold temperature (dashed) at magnetic fields ranging from 5×10^{16}–10^{18} G in decreasing order. As the magnetic field decreases, the threshold temperature decreases, both absolutely and relative to $T_{\rm c}$, for $\mu > 311$ MeV. This is the region where DCDW is inhomogeneous, so the LP instability returns in the limit $B \to 0$. This figure is adapted from Figure 5 of Ref. [36].

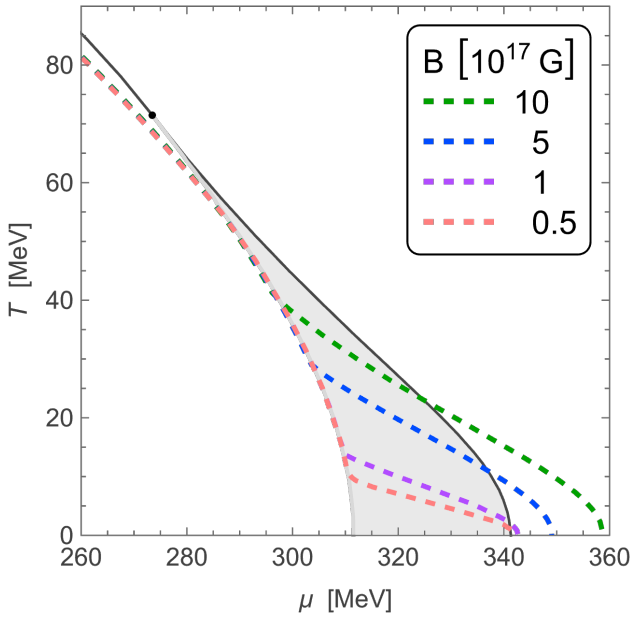


Figure 8. Threshold temperature curves of Figure 7 superposed on the phase diagram of DCDW. The gray shaded region indicates where the DCDW phase is inhomogeneous. The threshold temperature for MDCDW vanishes as $B \to 0$ only over the region of chemical potentials where the inhomogeneous phase is favored in the limit. At smaller μ, the threshold temperature stabilizes along the homogeneous–inhomogeneous phase boundary. This figure is adapted from Figure 6 of Ref. [36].

Let us again highlight the crucial role of the $\beta_{i,j}$ coefficients, and hence the topological aspect of MDCDW, in removing the LP instability. Recall that at sixth order, setting the $\beta_{i,j}$ coefficients to zero makes the expression for $v_\perp^2$ in Equation (33) identical to the expression in Equation (35), which is a stationary equation. Thus, $v_\perp^2$ vanishes and the LP instability appears. Strikingly, the same phenomenon occurs at Nth order, which can be shown directly from the Nth-order version of $v_\perp^2$ in Equation (46) and the corresponding stationary equation. Since having nonzero $\beta_{i,j}$ coefficients results from the spectral asymmetry of the LLL, which in turn arises from a combination of the magnetic field and the form of the MDCDW ansatz, one cannot conclude that magnetic fields alone are sufficient for single-modulated phases to avoid the LP instability in general.

6. Convergence of the GL Expansion

In this section, we show that the GL expansion for MDCDW converges in the region where $|m| + |b| < \sqrt{\mu^2 + (\pi T)^2}$. Note that, while on physical grounds m and b have been assumed to be real and positive throughout the paper, in this section, we consider them formally as complex variables, which is more natural in the context of analyzing power series convergence. The results of this section still apply to the case where m and b are restricted to be real and positive, in which case, the absolute value signs in $|m| + |b| < \sqrt{\mu^2 + (\pi T)^2}$ are simply redundant.

6.1. Convergence for $b = B = 0$

We begin by reviewing the result found in Ref. [37] for the simpler case of a homogeneous condensate in the absence of a magnetic field, i.e., $b = B = 0$. In this case, the expansion in Equation (17) reduces to

$$\Omega = \alpha_{0,0} + \alpha_{2,0} m^2 + \alpha_{4,0} m^4 + \alpha_{6,0} m^6 + \cdots , \tag{47}$$

where we have removed the sixth-order truncation. Since m only appears with even powers, it is convenient to re-express Equation (47) in terms of $x = m^2$ and $A_{N,0} = \alpha_{2N,0}$:

$$\Omega = A_{0,0} + A_{1,0}x + A_{2,0}x^2 + A_{3,0}x^3 + \cdots . \tag{48}$$

If the series in Equation (48) has radius of convergence r_x; this means it converges when $|x| < r_x$. Since the series in Equation (47) is the same except with $x \to m^2$ (as the coefficients are identical), it follows that this series converges when $|m^2| < r_x$, equivalently $|m| < \sqrt{r_x}$. In other words, if we denote the radii of convergence of the series in Equations (47) and (48) by r_m and r_x respectively, then we have

$$r_m = \sqrt{r_x}. \tag{49}$$

Since the convergence behavior of an infinite series is insensitive to any finite number of initial terms, we need only consider the $N \geq 3$ case. For such N, Equations (19)–(23) give

$$A_{N,0} = A^{\text{vac}}_{N,0} + A^{\text{med}}_{N,0} \tag{50}$$

$$A^{\text{vac}}_{N,0} = \frac{1}{N!}\frac{N_f N_c}{(2\pi)^2}\frac{(-1)^{N-1}}{2N-4} \tag{51}$$

$$A^{\text{med}}_{N,0} = \frac{1}{N!}\frac{N_f N_c}{(2\pi)^2}\frac{(-1)^{N-1}}{(N-2)!}\left(\frac{\beta}{4\pi}\right)^{2N-4} \text{Re}\left[\psi^{(2N-4)}\left(\frac{1}{2} + i\frac{\beta\mu}{2\pi}\right)\right]. \tag{52}$$

The radius of convergence of Equation (48), denoted r_x, is given by the Cauchy–Hadamard formula,

$$r_x^{-1} = \limsup_{N\to\infty} |A_{N,0}|^{1/N}. \tag{53}$$

It is easy to show that $\lim_{N\to\infty} |A^{\text{vac}}_{N,0}|^{1/N} = 0$, and consequently that $\limsup |A_{N,0}|^{1/N} = \limsup |A^{\text{med}}_{N,0}|^{1/N}$. A more difficult argument [37] shows the second equality in

$$\limsup_{N\to\infty} |A_{N,0}|^{1/N} = \limsup_{N\to\infty} |A^{\text{med}}_{N,0}|^{1/N} = [\mu^2 + (\pi T)^2]^{-1}, \tag{54}$$

hence, $r_x = \mu^2 + (\pi T)^2$. It follows from Equation (49) that the radius of convergence of Equation (47), denoted r_m, is given by $r_m = \sqrt{\mu^2 + (\pi T)^2}$.

6.2. Convergence for $b > 0, B = 0$

In the absence of a magnetic field, only the $|eB|^0$ terms in Equations (19)–(23) survive (in particular, the $\beta_{i,j}$ coefficients vanish, and the EM series in the formula for the α coefficients reduces from an asymptotic series to a single term that describes the free energy exactly). The expansion in Equation (17) reduces to

$$\Omega = \alpha_{0,0} + \alpha_{2,0}m^2 + \alpha_{4,0}m^4 + \alpha_{4,2}m^2b^2 + \alpha_{6,0}m^6 + \alpha_{6,2}m^4b^2 + \alpha_{6,4}m^2b^4 + \cdots . \tag{55}$$

Extending the notation of Section 6.1, we define $x = m^2$, $y = b^2$, and $A_{N,k} = \alpha_{2N,2k}$, giving

$$\Omega = A_{0,0} + A_{1,0}x + A_{2,0}x^2 + A_{2,1}xy + A_{3,0}x^3 + A_{3,1}x^2y + A_{3,2}xy^2 + \cdots . \tag{56}$$

Analyzing the convergence properties of the expansion in Equation (56) requires the theory of power series in several variables, which is not as simple as the single-variable case. We review the relevant mathematical background in Appendix A. Briefly, the multivariable analog of the Cauchy–Hadamard formula expresses a relation between the so-called conjugate radii of convergence, which taken together describe the boundary of the domain

of convergence. The general formula is given in Equation (A1); applied to Equation (56), it becomes

$$\limsup_{N\to\infty} \max_{0\le k\le N-1} |A_{N,k} r_x^{N-k} r_y^k|^{1/N} = 1, \tag{57}$$

where r_x and r_y denote conjugate radii of convergence in x and y. For reasons analogous to those leading up to Equation (49), if we let r_m and r_b denote the conjugate radii of convergence of m and b in Equation (55), then we have

$$r_m = \sqrt{r_x}, \qquad r_b = \sqrt{r_y}. \tag{58}$$

A crucial property of the coefficient formulas in Equations (19)–(23) is that all coefficients α_{n,n_b} or β_{n,n_b} at fixed n but varying n_b are related by numerical pre-factors. For the α coefficients, we have,

$$\alpha_{n,n_b} = c_{n,n_b}\alpha_{n,0} \tag{59}$$

$$c_{n,n_b} = \frac{(n/2)!}{(n_m/2)!n_b!}\frac{(n-2)!!}{(n_m-2)!!}2^{n_b/2}. \tag{60}$$

We can therefore define the numbers $C_{N,k}$ such that $A_{N,k} = C_{N,k}A_{N,0}$, and after some manipulations, we find

$$C_{N,k} = c_{2N,2k} = \frac{N-k}{N}\left(\frac{N!}{(N-k)!}\right)^2 \frac{2^{2k}}{(2k)!}, \qquad k = 0,\ldots,N-1. \tag{61}$$

The Cauchy–Hadamard formula now reads

$$r_x \cdot \limsup_{N\to\infty} \left(|A_{N,0}|^{1/N} \max_{0\le k\le N-1} |C_{N,k}(r_y/r_x)^k|^{1/N} \right) = 1. \tag{62}$$

By a careful argument involving the squeeze theorem (see Appendix B), one can show that

$$\lim_{N\to\infty} \max_{0\le k\le N-1} |C_{N,k}(r_y/r_x)^k|^{1/N} = \left(1+\sqrt{r_y/r_x}\right)^2, \tag{63}$$

and this result [in particular, the fact that Equation (63) is a limit and not merely a lim sup] combined with Equations (54) and (62) shows that

$$r_x \cdot \frac{1}{\mu^2+(\pi T)^2} \cdot \left(1+\sqrt{r_y/r_x}\right)^2 = 1. \tag{64}$$

A simple rearrangement gives

$$\sqrt{r_x} + \sqrt{r_y} = \sqrt{\mu^2+(\pi T)^2}, \tag{65}$$

which by Equation (58) is equivalent to the claim that $r_m + r_b = \sqrt{\mu^2+(\pi T)^2}$. This means the expansion in Equation (55) converges in the region where

$$|m| + |b| < \sqrt{\mu^2+(\pi T)^2}. \tag{66}$$

The ground state order parameters of MDCDW satisfy Equation (66) over a large region of parameter space, indicated by the green shaded regions in the bottom-right panels of Figure 1 ($B = 0$) and Figure 2 ($B = 1.5\times 10^{18}$ G). This justifies using very-high-order GL expansions to obtain accurate results on the phase diagrams of MDCDW.

6.3. Convergence for $b > 0, B > 0$

When a magnetic field is introduced, the coefficient formulas in Equations (19)–(23) are complicated by the appearance of an EM series, which is divergent. Thus, there is already no hope of that the GL expansion defined by these coefficients converges exactly to the free energy given in Equations (9)–(13). However, we may still analyze the convergence of the GL expansion in a rigorous sense by truncating the EM series at some finite order p_0. Consider the EM expansion of the free energy,

$$\Omega = \frac{m^2}{4G} + \sum_f \sum_{p=0}^{\infty} \Omega^{f,(p)}, \tag{67}$$

where each term $\Omega^{f,(p)}$ resulting from the EM formula contains a pre-factor of $|e_f B|^p$. The expansion in Equation (67) is divergent, but for sufficiently small fields, the first few terms decrease rapidly and give an accurate result. Moreover, the odd terms beyond $p = 1$ always vanish in the EM formula, so the terms beyond $p = 2$ contain pre-factors that increase by powers of $|e_f B|^2$. For a field $B = 10^{18}$ G, the dimensionless version of this quantity for the up quark term is $(|e_u B|/\Lambda^2)^2 \approx 9 \times 10^{-5} \ll 1$. Importantly, each term $\Omega^{f,(p)}$ is finite and completely well defined, and it is only the infinite sum in Equation (67) that is ill defined.

Since the coefficient formulas are effectively derived from Equation (67), the formula in Equation (19) with a truncated EM order $p = p_0$ gives the α coefficient for a GL expansion of (67) also truncated at $p = p_0$. With this truncation in place, the GL expansion naturally separates into several series, one for each contribution of order $|e_f B|^p$ to the free energy.

For even p, the pth-order EM contribution to the GL expansion is

$$\Omega^{(p)} = \alpha^{(p)}_{0,0} + \alpha^{(p)}_{2,0} m^2 + \alpha^{(p)}_{4,0} m^4 + \alpha^{(p)}_{4,2} m^2 b^2 + \alpha^{(p)}_{6,0} m^6 + \alpha^{(p)}_{6,2} m^4 b^2 + \alpha^{(p)}_{6,4} m^2 b^4 + \cdots, \tag{68}$$

where $\alpha^{(p)}_{n,n_b}$ is just the expression in Equation (19) with the EM sum $\sum_{p=0,2,4,\ldots}$ replaced by the single term of order p. The terms with $\beta_{i,j}$ coefficients do not contribute to Equation (68) because they contribute only at linear order in $|e_f B|$. This linear term with $p = 1$ is the only odd-order term in the EM expansion, and its contribution to the GL expansion is

$$\Omega^{(1)} = \beta_{3,1} m^2 b + \beta_{5,1} m^4 b + \beta_{5,3} m^2 b^3 + \cdots. \tag{69}$$

Here, the α terms do not contribute, as can be seen from Equation (19).

It is fairly straightforward to extend the calculations of the previous section for $B = 0$ to the above expansions in Equations (68) and (69). In both cases, the analogous formulas remain essentially unchanged apart from superficial details, and the final result is the same as before: Each contribution to the GL expansion converges in the region where $|m| + |b| < \sqrt{\mu^2 + (\pi T)^2}$. We offer a few more details on this calculation in Appendix C.

7. Summary and Outlook

In this review, we have shown that the tendency toward formation of the MDCDW phase is significantly enhanced by strong magnetic fields. Such fields increase the condensate magnitude and critical temperature, widening the range of parameter space in the μ-T plane where the condensate is energetically favored over the chirally symmetric state. Magnetic fields also stabilize MDCDW against thermal phonon fluctuations. We have demonstrated how a high-order GL expansion can be used to study these effects, and we proved that the expansion converges over a large region of parameter space. The $\beta_{i,j}$ coefficients in this expansion arise due to the spectral asymmetry of the LLL, a topological effect that appears due to a combination of the magnetic field and the condensate background. Our GL-based analysis clearly shows that these $\beta_{i,j}$ coefficients, and hence the

phase's topological properties, are responsible for its resilience against high temperatures. These thermal properties make MDCDW a plausible candidate phase for the interiors of neutron stars.

Several open questions about MDCDW are worth exploring in future work. The first is whether the charge-neutral, β-equilibrated version of MDCDW is favored in a similar range of parameter space. Taking charge neutrality into account is necessary to describe the environment of neutron stars more realistically. For charge-neutral MDCDW, one could also compute the equation of state (EOS), speed of sound, and transport properties, and check whether the results are consistent with neutron star observations. A recent study [45] investigated these questions for the neutral DCDW phase (in the absence of a magnetic field) and found that it becomes disfavored at NS densities and has too soft an EOS to produce realistic NSs. We have seen here, however, that magnetic fields have a significant effect on the condensate, making it more robust than the DCDW phase.

A recent work [31] studied the sensitivity of inhomogeneous phases in the NJL model to the regularization procedure used on the divergent vacuum contribution to the free energy. It was found that the existence of such phases depends strongly on the regularization scheme, casting doubt on the physical interpretation of results derived from such models. However, the topological mechanisms behind MDCDW's phase structure and thermal stability are unrelated to the vacuum regularization, so it is natural to suspect MDCDW may be immune to such scheme sensitivity. To assess this claim, it would be interesting to repeat calculations similar to those performed here but for different regularization schemes, such as Pauli Villars and a simple momentum cutoff, and to check whether results remain consistent across the different methods.

Another important direction for future research is to examine the effects of other types of thermal fluctuations apart from the low-energy phonon fluctuations considered here. In this paper, we have restricted our focus to the effect of thermal phonon fluctuations at second order coming from the IR region only, because this is the dominant contribution that leads to the LP instability. However, a more complete analysis should consider contributions beyond the IR region and from higher-order terms in the fluctuation, as the $\mathcal{O}(u^3)$ term is known at least in the case of smectic liquid crystals to introduce anharmonic effects that modify the scaling behavior [46,47]. One could also carefully study the effects of charged pion fluctuations, incorporate interactions between quarks, phonons, and pions, and take into account the effect of nonzero quark masses.

Finally, it would be interesting to explore the extent to which these results generalize to other condensates in the presence of a background vector field. It was argued in Ref. [36] that the spectral asymmetry of MDCDW can be traced back to the simultaneous existence of a time reversal (T) symmetry-breaking ansatz and a vector structure that breaks rotational symmetry. It was conjectured that when a magnetic field is present, the following three features become equivalent and are sufficient for a phase to avoid the LP instability: (1) a T-breaking ground state, (2) an anomalous baryon number, and (3) an asymmetric fermion spectrum. If true, the mechanism that stabilizes MDCDW may have broader implications for dense QCD and condensed matter physics.

Funding: This research received no external funding.

Data Availability Statement: No new data were created or analyzed in this study. Data sharing is not applicable to this article.

Conflicts of Interest: The author declares no conflicts of interest.

Abbreviations

The following abbreviations are used in this manuscript:

EM	Euler–Maclaurin
GL	Ginzburg–Landau
HLL	Higher Landau level
IP	Inhomogeneous phase
IR	Infrared
LLL	Lowest Landau level
LP	Landau–Peierls
(M)DCDW	(Magnetic) dual chiral density wave
NJL	Nambu–Jona-Lasinio
NS	Neutron star
QCD	Quantum chromodynamics
RKC	Real kink crystal
UV	Ultraviolet

Appendix A. Review of Power Series in Several Variables

The theory of power series in several variables is more complicated than in the single-variable case (see, e.g., Ref. [48]). Recall that a power series $\sum_n c_n z^n$ in one complex variable always converges absolutely in some open disc $\{z \in \mathbb{C} : |z| < r\}$, diverges for all $|z| > r$, and may either converge or diverge for $|z| = r$. In several variables, one might expect regions of convergence to be Euclidean balls, which are of the form $\{z \in \mathbb{C}^n : |z| < r\}$, or polydiscs, which are of the form $\{z \in \mathbb{C}^n : |z_1| < r_1, \ldots, |z_n| < r_n\}$, but in fact, regions of convergence need not be either of these.

The *set of convergence* S of a series in one or more variables denotes the set of all points in $\mathbb{C}^n$ for which the series converges (perhaps conditionally), whereas the *domain of convergence* S° is the topological interior of S. It can be shown that convergence in S° is absolute. In several variables, S° is in general a union of polydiscs, also known as a *complete Reinhardt domain*; these are precisely the open sets $A \subseteq \mathbb{C}$ such that $(z_1, \ldots, z_n) \in A \implies (\lambda_1 z_1, \ldots \lambda_n z_n) \in A$ for all $|\lambda_1|, \ldots, |\lambda_n| \leq 1$. Any such region is in fact a union of certain extremal polydiscs called *polydiscs of convergence*, defined as polydiscs contained in S° such that no strictly larger polydisc is contained in S°. In other words, a polydisc $U(r) = U(r_1, \ldots, r_n) = \{z \in \mathbb{C} : |z_1| < r_1, \ldots, |z_n| < r_n\}$ is a polydisc of convergence if $U(r) \subseteq S^\circ$ but $U(r') \nsubseteq S^\circ$ for any r' with $r'_k \geq r_k$ for all $k = 1, \ldots n$ where at least one inequality is strict. If $U(r)$ is a polydisc of convergence, the radii $r = (r_1, \ldots, r_n)$ are called *conjugate radii of convergence*.

A simple example is given by the double series $\sum_{n=0}^{\infty} z_1^n z_2^n$, whose domain of convergence is the region where $|z_1 z_2| < 1$. This Reinhardt domain may be depicted as the region in the $|z_1|$-$|z_2|$ quarter-plane bounded above by the hyperbola $|z_1| \cdot |z_2| = 1$; its conjugate radii of convergence are the pairs $(r_1, 1/r_1)$ for all $r_1 \in (0, \infty)$.

The higher-dimensional analog of the Cauchy–Hadamard formula expresses a relation between conjugate radii of convergence: For a multivariable series $\sum_{|k|=0} c_k z^k$, where $k = (k_1, \ldots, k_n)$ is a multi-index, $|k| = k_1 + \cdots + k_n$, and $z^k = z_1^{k_1} \ldots z_n^{k_n}$, the conjugate radii of convergence $r = (r_1, \ldots, r_n)$ satisfy

$$\limsup_{|k| \to \infty} |c_k r^k|^{1/|k|} = 1, \tag{A1}$$

where again we use multi-index notation, so that $r^k = r_1^{k_1} \ldots r_n^{k_n}$. Thus, in the multivariable case, we obtain not a single radius of convergence, but rather a set of conjugate radii of convergence characterized by Equation (A1), which together form the boundary of the

domain of convergence. In Section 6, we use Equation (A1) to show that the conjugate radii of convergence r_m and r_b of the GL expansion for MDCDW satisfy the relation $r_m + r_b = \sqrt{\mu^2 + (\pi T)^2}$, which is equivalent to the claim that the expansion converges in the region where $|m| + |b| < \sqrt{\mu^2 + (\pi T)^2}$.

Appendix B. Limit Calculation for Domain of Convergence

In this appendix, we prove the result stated in Equation (63),

$$\lim_{N\to\infty} \max_{0\le k\le N-1} |C_{N,k}(r_y/r_x)^k|^{1/N} = \left(1 + \sqrt{r_y/r_x}\right)^2. \tag{A2}$$

For convenience, we define

$$h = \sqrt{r_y/r_x} \tag{A3}$$

$$f_N(k) = C_{N,k}(r_y/r_x)^k \tag{A4}$$

$$C_N = \max_{k=0,\ldots,N-1} f_N(k), \tag{A5}$$

and our goal is to compute $\lim_{N\to\infty} C_N^{1/N}$. The strategy is to define upper and lower bounds $C_N^- \le C_N \le C_N^+$ and show that $\lim(C_N^-)^{1/N} = \lim(C_N^+)^{1/N} = (1+h)^2$. From the definitions, we have

$$f_N(k) = \frac{N-k}{N}\left(\frac{N!}{(N-k)!}\right)^2 \frac{(2h)^{2k}}{(2k)!}, \qquad k = 0,\ldots,N-1. \tag{A6}$$

Using the inequality

$$e^{x\ln x - x} \le x! \le e^{(x+1)\ln(x+1)-x} \quad (x \ge 0), \tag{A7}$$

where $x! = \Gamma(x+1)$, we first obtain upper and lower bounds $f_N^{\pm}(k)$ as follows,

$$f_N^+(k) = \exp\left[2(N+1)\ln(N+1) - 2(N-k)\ln(N-k) - 2k\ln(2k) + 2k\ln(2h)\right] \tag{A8}$$

$$f_N^-(k) = \frac{1}{N}\exp\left[2N\ln N - 2(N-k+1)\ln(N-k+1) - (2k+1)\ln(2k+1) + 2k\ln(2h)\right], \tag{A9}$$

and we note that $0 \le f_N^-(k) \le f_N(k) \le f_N^+(k)$ for $k = 0,\ldots,N-1$.

Although $f_N(k)$ is defined only at $k = 0,\ldots,N-1$, the bounds $f_N^{\pm}(k)$ are defined for all $k \in [0, N)$. It is straightforward to check that f_N^+ is maximized at

$$k_0^+ = \frac{N}{1+1/h}. \tag{A10}$$

Defining

$$\begin{aligned} C_N^+ &= f_N^+(k_0^+) \\ &= [(1+1/N)(1+h)]^{2N}(N+1)^2, \end{aligned} \tag{A11}$$

we see that C_N^+ is an upper bound for C_N,

$$\begin{aligned} C_N &= \max_{k=0,\ldots,N-1} f_N(k) \\ &\leq \max_{k=0,\ldots,N-1} f_N^+(k) \\ &\leq f_N^+(k_0^+) \\ &= C_N^+, \end{aligned} \tag{A12}$$

and also

$$\lim_{N\to\infty} (C_N^+)^{1/N} = (1+h)^2. \tag{A13}$$

To obtain a lower bound for C_N, we first note that f_N^- is maximized at

$$k_0^- = \frac{N+1-1/2h}{1+1/h}. \tag{A14}$$

Let

$$C_N^- = f_N^-(k_0^- + 1). \tag{A15}$$

For sufficiently large N, we have $k_0^- \in [0, N-2]$, and hence there must exist an integer $n \in [k_0^-, k_0^- + 1]$ such that $0 \leq n \leq N-1$. Since f_N^- is decreasing on $[k_0^-, k_0^- + 1]$, we have

$$\begin{aligned} C_N^- &= f_N^-(k_0^- + 1) \\ &\leq f_N^-(n) \\ &\leq f_N(n) \\ &\leq \max_{k=0,\ldots,N-1} f_N(k) \\ &= C_N. \end{aligned} \tag{A16}$$

From the definition of f_N^-, we find

$$\begin{aligned} C_N^- = \exp[&(2N-1)\ln N - 2(N-k_0^-)\ln(N-k_0^-) \\ &- (2k_0^- + 3)\ln(2k_0^- + 3) + 2(k_0^- + 1)\ln(2h)], \end{aligned} \tag{A17}$$

and it is now a straightforward but tedious exercise to show that $\lim_{N\to\infty}(C_N^-)^{1/N} = (1+h)^2$. It then follows from the squeeze theorem that $\lim_{N\to\infty} = C_N^{1/N} = (1+h)^2$, as claimed.

Appendix C. GL Convergence for $B > 0$

In this appendix, we show that the higher-order EM contributions to the GL expansion (i.e., the contributions coming from terms proportional to $|eB|^p$ for $p > 0$) have the same radius of convergence as that of the $p = 0$ term.

To calculate the radius of convergence of Equation (68), we define $A_{N,k}^{(p)} = \alpha_{2N,2k}^{(p)}$ and write

$$\Omega^{(p)} = A_{0,0}^{(p)} + A_{1,0}^{(p)} x + A_{2,0}^{(p)} x^2 + A_{2,1}^{(p)} xy + A_{3,0}^{(p)} x^3 + A_{3,1}^{(p)} x^2 y + A_{3,2}^{(p)} xy^2 + \cdots, \tag{A18}$$

following the previous notation where $x = m^2$ and $y = b^2$. Again, the convergence behavior can be determined by considering the $k = 0$ terms for sufficiently large N, and

then observing that the previous relation $A^{(p)}_{N,k} = C_{N,k} A^{(p)}_{N,0}$ remains unchanged for $p > 0$, with $C_{N,k}$ exactly as in Equation (61). For large N, we have

$$A^{(p)}_{N,0} = A^{(p),\mathrm{vac}}_{N,0} + A^{(p),\mathrm{med}}_{N,0} \tag{A19}$$

$$A^{(p),\mathrm{vac}}_{N,0} = \frac{1}{N!} \frac{N_c(\frac{2^p+1}{3^p})|eB|^p}{(2\pi)^2} \frac{B^-_p}{p!} \frac{(-1)^{N-1}2^p}{2N+2p-4} \tag{A20}$$

$$A^{(p),\mathrm{med}}_{N,0} = \frac{1}{N!} \frac{N_c(\frac{2^p+1}{3^p})|eB|^p}{(2\pi)^2} \frac{B^-_p}{p!} \frac{(-1)^{N-1}2^p}{(N+p-2)!} \left(\frac{\beta}{4\pi}\right)^{2N+2p-4} \mathrm{Re}\, \psi^{(2N+2p-4)}\left(\frac{1}{2} + i\frac{\beta\mu}{2\pi}\right). \tag{A21}$$

It is straightforward to check that the appearance of p in Equations (A20) and (A21) does not significantly change the ensuing calculation of the radius of convergence, and one finds the same result,

$$\limsup_{N\to\infty} |A^{(p)}_{N,0}|^{1/N} = \frac{1}{\mu^2 + (\pi T)^2}. \tag{A22}$$

Since the $C_{N,k}$ appearing in $A^{(p)}_{N,k} = C_{N,k} A^{(p)}_{N,0}$ for even $p > 0$ are identical to those of the $p = 0$ case given by Equation (61), the rest of the calculation is the same as before. We find that each $|eB|^p$ contribution for even $p > 0$ converges for $|m| + |b| < \sqrt{\mu^2 + (\pi T)^2}$.

It remains to determine the domain of convergence of the linear-in-$|eB|$ contribution to the GL expansion. This is the only odd-order term in the EM series, and it enters the GL expansion only through the $\beta_{i,j}$ coefficients. Thus, its contribution to the GL expansion takes the form

$$\Omega^{(1)} = \beta_{3,1} m^2 b + \beta_{5,1} m^4 b + \beta_{5,3} m^2 b^3 + \cdots. \tag{A23}$$

Multiplying every term in a power series by the same number cannot affect whether the series converges, so we can factor out b from Equation (69) and then examine the convergence of the series multiplying b. Letting $x = m^2$, $y = b^2$, and $B_{N,k} = \beta_{2N+1,2k+1}$, we have

$$\Omega^{(1)} = b(B_{1,0}x + B_{2,0}x^2 + B_{2,1}x^2 y + \dots). \tag{A24}$$

We then compute

$$B_{N,0} = \frac{1}{N!} \frac{N_c|eB|}{(2\pi)^2} \frac{(-1)^{N-1}2}{(N-1)!} \left(\frac{\beta}{4\pi}\right)^{2N-1} \mathrm{Im}\left[\psi^{(2N-1)}\left(\frac{1}{2} + i\frac{\beta\mu}{2\pi}\right)\right] \tag{A25}$$

$$\frac{B_{N,k}}{B_{N,0}} = \frac{N-k}{N} \left(\frac{N!}{(N-k)!}\right)^2 \frac{1}{(2k+1)!} 2^{2k} \tag{A26}$$

Despite some superficial differences with the even p case, the associated calculations are essentially unchanged, and in particular, we find the same results

$$\limsup_{N\to\infty} |B_{N,0}|^{1/N} = \frac{1}{\mu^2 + (\pi T)^2} \tag{A27}$$

and

$$\lim_{N\to\infty} \max_{k=0,\dots,N-1} \left| \frac{B_{N,k}}{B_{N,0}} (r_y/r_x)^k \right|^{1/N} = \left(1 + \sqrt{r_y/r_x}\right)^2, \tag{A28}$$

leading to the same domain of convergence.

https://doi.org/10.3390/universe12070208

Notes

[1] It is interesting that the GL solutions are sometimes still accurate slightly outside the convergence region, e.g., for 280 MeV $< \mu <$ 314 MeV in the top-right panel of Figure 2. To partially explain this phenomenon, we note that the behavior of a local minimum near the edge of a convergence region is nontrivial. While solutions inside the convergence region are guaranteed to be well approximated at sufficiently high order, it does not follow that a particular high-order expansion must fail to approximate solutions outside the convergence region.

[2] Some formulas in this section are only apparently different from those appearing in [33,36,44], because here we use b as the order parameter rather than $q = 2b$. In particular, the squared velocities defined in this section differ from the previous ones by a factor of 4.

References

1. Lai, D.; Shapiro, S.L. Cold Equation of State in a Strong Magnetic Field: Effects of Inverse Beta-Decay. *Astrophys. J.* **1991**, *383*, 745. [CrossRef] [PubMed]
2. Ferrer, E.J.; de la Incera, V.; Keith, J.P.; Portillo, I.; Springsteen, P.L. Equation of state of a dense and magnetized fermion system. *Phys. Rev. C* **2010**, *82*, 065802. [CrossRef]
3. Nambu, Y.; Jona-Lasinio, G. Dynamical Model of Elementary Particles Based on an Analogy with Superconductivity. I. *Phys. Rev.* **1961**, *122*, 345–358. [CrossRef]
4. Nambu, Y.; Jona-Lasinio, G. Dynamical Model of Elementary Particles Based on an Analogy with Superconductivity. II. *Phys. Rev.* **1961**, *124*, 246–254. [CrossRef]
5. Buballa, M.; Carignano, S. Inhomogeneous chiral phases away from the chiral limit. *Phys. Lett. B* **2019**, *791*, 361–366. [CrossRef]
6. Grüner, G. The dynamics of spin-density waves. *Rev. Mod. Phys.* **1994**, *66*, 1–24. [CrossRef]
7. Maeda, K.; Hatsuda, T.; Baym, G. Antiferrosmectic ground state of two-component dipolar Fermi gases: An analog of meson condensation in nuclear matter. *Phys. Rev. A* **2013**, *87*, 021604. [CrossRef]
8. Fulde, P.; Ferrell, R.A. Superconductivity in a Strong Spin-Exchange Field. *Phys. Rev.* **1964**, *135*, A550–A563. [CrossRef]
9. Larkin, A.I.; Ovchinnikov, Y.N. Nonuniform State of Superconductors. *Zh. Eksp. Teor. Fiz.* **1964**, *47*, 1136–1146.
10. Overhauser, A.W. Structure of Nuclear Matter. *Phys. Rev. Lett.* **1960**, *4*, 415–418. [CrossRef]
11. Deryagin, D.V.; Grigoriev, D.Y.; Rubakov, V.A. Standing Wave Ground State in High Density, Zero Temperature QCD at Large N_C. *Int. J. Mod. Phys. A* **1992**, *7*, 659–681. [CrossRef]
12. Kutschera, M.; Broniowski, W.; Kotlorz, A. Quark matter with neutral pion condensate. *Phys. Lett. B* **1990**, *237*, 159–163. [CrossRef]
13. Nakano, E.; Tatsumi, T. Chiral symmetry and density waves in quark matter. *Phys. Rev. D* **2005**, *71*, 114006. [CrossRef]
14. Nickel, D. Inhomogeneous phases in the Nambu–Jona-Lasinio and quark-meson model. *Phys. Rev. D* **2009**, *80*, 074025. [CrossRef]
15. Nickel, D. How Many Phases Meet at the Chiral Critical Point? *Phys. Rev. Lett.* **2009**, *103*, 072301. [CrossRef] [PubMed]
16. Alford, M.G.; Schmitt, A.; Rajagopal, K.; Schäfer, T. Color superconductivity in dense quark matter. *Rev. Mod. Phys.* **2008**, *80*, 1455–1515. [CrossRef]
17. Anglani, R.; Casalbuoni, R.; Ciminale, M.; Ippolito, N.; Gatto, R.; Mannarelli, M.; Ruggieri, M. Crystalline color superconductors. *Rev. Mod. Phys.* **2014**, *86*, 509–561. [CrossRef]
18. Kojo, T.; Hidaka, Y.; McLerran, L.; Pisarski, R.D. Quarkyonic chiral spirals. *Nucl. Phys. A* **2010**, *843*, 37–58. [CrossRef]
19. Başar, G.m.c.; Dunne, G.V.; Thies, M. Inhomogeneous condensates in the thermodynamics of the chiral NJL_2 model. *Phys. Rev. D* **2009**, *79*, 105012. [CrossRef]
20. Abuki, H.; Ishibashi, D.; Suzuki, K. Crystalline chiral condensates off the tricritical point in a generalized Ginzburg-Landau approach. *Phys. Rev. D* **2012**, *85*, 074002. [CrossRef]
21. Carignano, S.; Buballa, M. Two-dimensional chiral crystals in the Nambu-Jona-Lasinio model. *Phys. Rev. D* **2012**, *86*, 074018. [CrossRef]
22. Peierls, R. Bemerkungen über Umwandlungstemperaturen. *Helv. Phys. Acta* **1934**, *7*, 81.
23. Peierls, R. Quelques propriétés typiques des corps solides. *Ann. L'Institut Henri Poincaré* **1935**, *5*, 177–222.
24. Landau, L.D. On the theory of phase transitions. I. *Phys. Z. Sowjet.* **1937**, *11*, 26.
25. Landau, L.D. On the theory of phase transitions. II. *Zh. Eksp. Teor. Fiz.* **1937**, *7*, 627.
26. Hidaka, Y.; Kamikado, K.; Kanazawa, T.; Noumi, T. Phonons, pions, and quasi-long-range order in spatially modulated chiral condensates. *Phys. Rev. D* **2015**, *92*, 034003. [CrossRef]
27. Ferrer, E.; de la Incera, V. Novel topological effects in dense QCD in a magnetic field. *Nucl. Phys. B* **2018**, *931*, 192–215. [CrossRef]
28. Tatsumi, T.; Nishiyama, K.; Karasawa, S. Novel Lifshitz point for chiral transition in the magnetic field. *Phys. Lett. B* **2015**, *743*, 66–70. [CrossRef]
29. Buballa, M. NJL-model analysis of dense quark matter. *Phys. Rep.* **2005**, *407*, 205–376. [CrossRef]
30. Klevansky, S.P. The Nambu-Jona-Lasinio model of quantum chromodynamics. *Rev. Mod. Phys.* **1992**, *64*, 649–708. [CrossRef]

31. Pannullo, L.; Wagner, M.; Winstel, M. Regularization effects in the Nambu–Jona-Lasinio model: Strong scheme dependence of inhomogeneous phases and persistence of the moat regime. *Phys. Rev. D* **2024**, *110*, 076006. [CrossRef]
32. Frolov, I.E.; Zhukovsky, V.C.; Klimenko, K.G. Chiral density waves in quark matter within the Nambu–Jona-Lasinio model in an external magnetic field. *Phys. Rev. D* **2010**, *82*, 076002. [CrossRef]
33. Gyory, W. Phase Transitions and Thermal Stability of the Magnetic Dual Chiral Density Wave Phase in Cold, Dense QCD. Ph.D. Thesis, CUNY Graduate Center, New York, NY, USA, 2023.
34. Schwinger, J.S. On gauge invariance and vacuum polarization. *Phys. Rev.* **1951**, *82*, 664–679. [CrossRef]
35. Gyory, W.; de la Incera, V. Phase transitions and resilience of the magnetic dual chiral density wave phase at finite temperature and density. *Phys. Rev. D* **2022**, *106*, 016011. [CrossRef]
36. Ferrer, E.J.; Gyory, W.; de la Incera, V. Thermal phonon fluctuations and stability of the magnetic dual chiral density wave phase in dense QCD. *Phys. Rev. D* **2024**, *109*, 036023. [CrossRef]
37. Gyory, W.; Yamamoto, N. Convergence of Ginzburg–Landau Expansions: Superconductivity in the Bardeen–Cooper–Schrieffer Theory and Chiral Symmetry Breaking in the Nambu–Jona-Lasinio Model. *Prog. Theor. Exp. Phys.* **2024**, *2024*, 043D01. [CrossRef]
38. Endrizzi, A.; Perego, A.; Fabbri, F.M.; Branca, L.; Radice, D.; Bernuzzi, S.; Giacomazzo, B.; Pederiva, F.; Lovato, A. Thermodynamics conditions of matter in the neutrino decoupling region during neutron star mergers. *Eur. Phys. J. A* **2020**, *56*, 15. [CrossRef]
39. Ciolfi, R. The key role of magnetic fields in binary neutron star mergers. *Gen. Relativ. Gravit.* **2020**, *52*, 59 . [CrossRef]
40. Kiuchi, K.; Cerdá-Durán, P.; Kyutoku, K.; Sekiguchi, Y.; Shibata, M. Efficient magnetic-field amplification due to the Kelvin-Helmholtz instability in binary neutron star mergers. *Phys. Rev. D* **2015**, *92*, 124034. [CrossRef]
41. Tsokaros, A.; Ruiz, M.; Shapiro, S.L.; Uryū, K.b.o. Magnetohydrodynamic Simulations of Self-Consistent Rotating Neutron Stars with Mixed Poloidal and Toroidal Magnetic Fields. *Phys. Rev. Lett.* **2022**, *128*, 061101. [CrossRef] [PubMed]
42. Lee, T.G.; Nakano, E.; Tsue, Y.; Tatsumi, T.; Friman, B. Landau-Peierls instability in a Fulde-Ferrell type inhomogeneous chiral condensed phase. *Phys. Rev. D* **2015**, *92*, 034024. [CrossRef]
43. Pisarski, R.D.; Skokov, V.V.; Tsvelik, A.M. Fluctuations in cool quark matter and the phase diagram of quantum chromodynamics. *Phys. Rev. D* **2019**, *99*, 074025. [CrossRef]
44. Ferrer, E.J.; de la Incera, V. Absence of Landau-Peierls instability in the magnetic dual chiral density wave phase of dense QCD. *Phys. Rev. D* **2020**, *102*, 014010. [CrossRef]
45. Papadopoulos, O.; Schmitt, A. Nuclear chiral density wave in neutron stars? *J. Subat. Part. Cosmol.* **2025**, *4*, 100221. [CrossRef]
46. Grinstein, G.; Pelcovits, R.A. Anharmonic Effects in Bulk Smectic Liquid Crystals and Other "One-Dimensional Solids". *Phys. Rev. Lett.* **1981**, *47*, 856–859. [CrossRef]
47. Grinstein, G.; Pelcovits, R.A. Nonlinear elastic theory of smectic liquid crystals. *Phys. Rev. A* **1982**, *26*, 915–925. [CrossRef]
48. Shabat, B. *Introduction to Complex Analysis, Part II: Functions of Several Variables*; Introduction to Complex Analysis; American Mathematical Society: Providence, RI, USA, 1992.

Disclaimer/Publisher's Note: The statements, opinions and data contained in all publications are solely those of the individual author(s) and contributor(s) and not of MDPI and/or the editor(s). MDPI and/or the editor(s) disclaim responsibility for any injury to people or property resulting from any ideas, methods, instructions or products referred to in the content.